HHS Public Access

Author manuscript

Immunity. Author manuscript; available in PMC 2022 July 13.

Published in final edited form as:

Immunity. 2021 July 13; 54(7): 1392–1404.e10. doi:10.1016/j.immuni.2021.04.024.

Dipeptidyl Peptidase 9 Sets a Threshold for CARD8 Inflammasome Formation by Sequestering Its Active C-terminal Fragment

Humayun Sharif[1,2,7], **L. Robert Hollingsworth**[1,2,3,7], **Andrew R. Griswold**[4,5,7], **Jeffrey C. Hsiao**[5], **Qinghui Wang**[6], **Daniel A. Bachovchin**[5,6,*], **Hao Wu**[1,2,8,*]

[1]Department of Biological Chemistry and Molecular Pharmacology, Harvard Medical School, Boston, MA 02115, USA

[2]Program in Cellular and Molecular Medicine, Boston Children's Hospital, Boston, MA 02115, USA

[3]Program in Biological and Biomedical Sciences, Harvard Medical School, Boston, MA 02115, USA

[4]Weill Cornell/Rockefeller/Sloan Kettering Tri-Institutional MD-PhD Program, New York, NY, USA

[5]Pharmacology Program, Weill Cornell Graduate School of Medical Sciences, Memorial Sloan Kettering Cancer Center, New York, New York 10065, USA

[6]Chemical Biology Program, Memorial Sloan Kettering Cancer Center, New York, NY, USA

[7]These authors contributed equally

[8]Lead Contact

SUMMARY

CARD8 detects intracellular danger signals and forms a caspase-1 activating inflammasome. Like the related inflammasome sensor NLRP1, CARD8 autoprocesses into noncovalently associated N-terminal (NT) and C-terminal (CT) fragments, and binds the cellular dipeptidyl peptidases DPP8 and 9 (DPP8/9). Certain danger-associated signals, including the DPP8/9 inhibitor Val-boroPro

*Correspondence: wu@crystal.harvard.edu (H.W.), bachovcd@mskcc.org (D.A.B.).

AUTHOR CONTRIBUTIONS

H.W., H.S., and L.R.H. conceived the project idea and designed the study. L.R.H. designed constructs with H.S.' input. L.R.H. carried out preliminary expression and purification studies and purified the complexes. H.S. and L.R.H. made cryo-EM grids for data collection. L.R.H. screened grids and collected cryo-EM data. H.S. analyzed cryo-EM data with assistance from L.R.H. and performed model building and refinement for the DPP9-CARD8-WT complexes. L.R.H. analyzed cryo-EM data for the DPP9-CARD8-S297A complex. H.S. and L.R.H. designed mutants. L.R.H. and A.R.G. cloned mutants for *in vitro* and cell-based assays. A.R.G. performed all cell-based assays with assistance from J.C.H and Q.W. under D.A.B.'s supervision. A.R.G., L.R.H., H.S., H.W., and D.A.B. designed the experiments. L.R.H., A.R.G., D.A.B., and H.W. wrote the manuscript with input from all authors.

DECLARATION OF INTERESTS

H.W. is a co-founder of Ventus Therapeutics. The other authors declare no competing financial interests.

SUPPLEMENTAL INFORMATION

Supplemental information includes five figures and two tables and can be found with this article online.

(VbP) and HIV protease, induce proteasome-mediated N-terminal degradation, and thereby liberate the inflammasome-forming CT. Here we report cryo-EM structures of CARD8 bound to DPP9, revealing a repressive ternary complex consisting of DPP9, full-length CARD8, and CARD8-CT. Unlike NLRP1-CT, CARD8-CT does not interact with the DPP8/9 active site and is not directly displaced by VbP. However, larger DPP8/9 active-site probes can directly weaken this complex in vitro, and VbP itself nevertheless appears to disrupt this complex, perhaps indirectly, in cells. Thus, DPP8/9 inhibitors can activate the CARD8 inflammasome by promoting CARD8 N-terminal degradation, and by weakening ternary complex stability.

Graphical Abstract

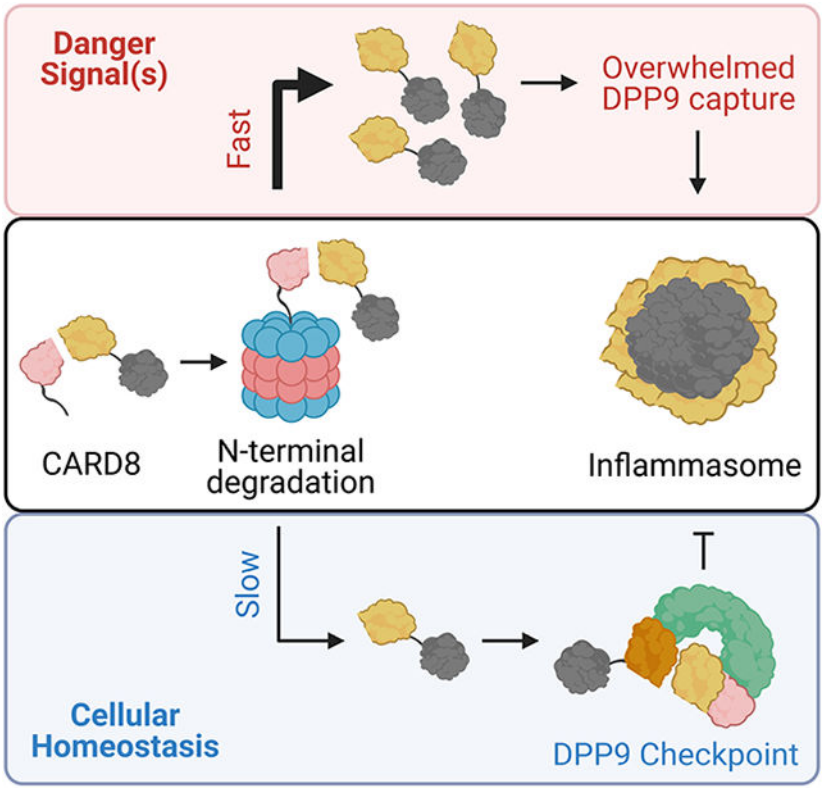

eTOC blurb

Inflammasomes are multiprotein complexes that execute pyroptosis in response to cytosolic danger signals. DPP9 regulates the CARD8 inflammasome by unknown mechanisms. Here, Sharif et al. report cryo-EM structures of CARD8 bound to DPP9 and show that this complex inhibits CARD8 inflammasome activation downstream of the proteasome.

Keywords

CARD8; NLRP1; DPP9; inflammasome; pyroptosis; Val-boroPro (VbP); cryo-EM; targeted degradation

INTRODUCTION

Canonical inflammasomes are cytosolic supramolecular signaling complexes that form in response to diverse pathogenic and endogenous danger signals and mediate inflammatory cytokine activation and pyroptotic cell death (Broz and Dixit; Martinon et al., 2002; Shen et al., 2019). Human CARD8 was recently identified to assemble one such inflammasome (Johnson et al., 2018), but unlike most other inflammasome sensors, CARD8 is not a member of the nucleotide-binding domain and leucine-rich repeat containing (NLR) family. It instead has an unusual function-to-find domain (FIIND) at the core of the protein flanked by a disordered N-terminal region that varies between isoforms (Bagnall et al., 2008) and a C-terminal caspase activation and recruitment domain (CARD) (Figure 1A). The FIIND and CARD of CARD8 share domain organization with those of one NLR inflammasome sensor, NLRP1. For both proteins, the FIIND possesses autoproteolytic activity to generate a noncovalent complex of the repressive N-terminal fragment (NT) that includes the ZU5 (found in ZO-1 and UNC5) subdomain of the FIIND, and the inflammatory C-terminal fragment (CT) that includes the UPA (conserved in UNC5, PIDD, and ankyrins) subdomain of the FIIND and the CARD (UPA-CARD) (D'Osualdo et al., 2011; Finger et al., 2012) (Figure 1A). The inflammatory CT must be released from the repressive NT for CARD8 activation (Johnson et al., 2018).

DPP8/9 inhibitors including Val-boroPro (VbP) activate the CARD8 inflammasome in human macrophages and resting lymphocytes, and the NLRP1 inflammasome in skin and airway epithelial cells (Johnson et al., 2020; Johnson et al., 2018; Linder et al., 2020; Robinson et al., 2020; Zhong et al., 2018). The mechanisms of DPP8/9 inhibitor-induced CARD8 and NLRP1 inflammasome activation have not yet been fully established. We recently discovered that DPP8/9 inhibitors induce the proteasomal degradation of the NT fragments (Chui et al., 2020; Chui et al., 2019), releasing the noncovalently associated CT fragments from autoinhibition (Figure 1B). In addition, CARD8 and NLRP1 directly bind to DPP8 and DPP9 (Griswold et al., 2019a; Zhong et al., 2018). Structural and biochemical studies of the NLRP1-DPP9 interaction recently revealed that DPP9 binding restrains NLRP1 activation by sequestering the freed NLRP1-CT fragment, and VbP activates human NLRP1, at least in part, by disrupting this interaction (Hollingsworth et al., 2020; Huang et al., 2020). In contrast, VbP does not directly disrupt the CARD8-DPP9 interaction (Griswold et al., 2019a), indicating mechanistic differences between the regulation of NLRP1 and CARD8 by DPP9.

Here, we investigated the structural and cellular mechanisms of CARD8 regulation by DPP9 and DPP8/9 inhibitors, revealing several differences from the recent complementary findings for NLRP1 (Hollingsworth et al., 2020; Huang et al., 2020). Most notably, we discovered that DPP9 binding also restrains the free CARD8-CT, but unlike NLRP1-CT, CARD8-CT does not closely interact with the DPP9 active site, explaining why DPP8/9 inhibitors do not directly displace CARD8-CT. However, we discovered that DPP8/9 inhibitors do destabilize this interaction in cells, possibly by competition from accumulated cellular DPP8/9 substrates. These data thus suggest that DPP8/9 inhibitors nevertheless induce CARD8 inflammasome activation via two separate mechanisms: 1) accelerated N-terminal degradation and 2) DPP9 complex disruption.

RESULTS

The CARD8-DPP9 Ternary Complex Structure Reveals CARD8-CT Sequestration by DPP9

We determined the cryo-EM structure of the co-expressed CARD8-DPP9 complex (Figure 1C) at a resolution of 3.3 Å (Figure S1, Table S1, S2A–B), which revealed 2 copies (molecules A and B) of CARD8 bound to a single DPP9 subunit, forming a $CARD8^{A}$-$CARD8^{B}$-DPP9 ternary complex (Figure 1D). Like for the NLRP1-DPP9 complex (Hollingsworth et al., 2020; Huang et al., 2020), molecule A has a full-length (FL) FIIND composed of the ZU5-UPA pair ($FIIND^{A}$), and molecule B contains only the UPA subdomain (UPA^{B}) from CT. Other domains of CARD8 were not visible in the EM density, likely due to their flexible linkage to the FIIND or their intrinsically disordered sequence composition (Chui et al., 2020). For $FIIND^{A}$, there is weak electron density around the autoprocessing site at residues 296–304 and these residues were not built. Unlike the NLRP1-DPP9 complex structure in which both monomers of the DPP9 dimer are each bound to 2 copies of NLRP1 (4:2 NLRP1:DPP9 stoichiometry) (Hollingsworth et al., 2020), the final CARD8-DPP9 map has a 2:2 CARD8:DPP9 stoichiometry in which one DPP9 monomer of the DPP9 dimer is not bound to CARD8. This result is explained by the abundance of the 2:2 CARD8:DPP9 complex particles (Figure S1C) over 4:2 CARD8:DPP9 complex particles (Figure S1D), likely reflecting under stoichiometric CARD8 expression relative to DPP9 but with no apparent functional significance.

The N-terminus of CARD8 UPA^{B} exhibits a notable difference from NLRP1 UPA^{B} despite the 50% sequence identity between CARD8 and NLRP1 FIINDs and the similar structural architecture of the ternary complexes (Figure 1E, S2A–B). Unlike the ordered N-terminus of NLRP1 UPA^{B} in the DPP9 active site (Hollingsworth et al., 2020), the N-terminus of CARD8 UPA^{B} does not insert into the DPP9 active site and is largely disordered (Figure 1E). The UPA^{B} did not have an associated $ZU5^{B}$, consistent with the larger amount of CARD8-CT than CARD8-NT in the co-eluted fraction of the CARD8-DPP9 complex (Figure 1C). This observation could be explained by N-terminal degradation of CARD8 (Chui et al., 2019; Johnson et al., 2018; Sandstrom et al., 2019) during normal protein turnover, which would free the noncovalently associated CT for ternary complex formation with $FIIND^{A}$ and DPP9.

When DPP9 monomers are aligned, the bound $FIIND^{A}$-UPA^{B} complex in CARD8 exhibits a modest shift relative to that in NLRP1, ~9° in rotation and ~1 Å in translation (Figure 1F), suggesting some differences in the exact binding mode to accommodate the sequence divergence. Among other ZU5 and UPA fold-containing proteins, the $FIIND^{A}$ β-sandwiches recapitulate the spatial relationship between ZU5 and UPA in the axonal guidance receptor Unc5b (Wang et al., 2009) but mimics the arrangement between ZU5(1) and UPA rather than the covalently linked ZU5(2) and UPA in the ZU5(1)-ZU5(2)-UPA module in ankyrin-B (Wang et al., 2012) (Figure S2C). However, neither ankyrin-B nor Unc5b contains an UPA-UPA interface seen in the $FIIND^{A}$-UPA^{B} complex. Thus, these data indicate that constitutively produced CARD8-CT is sequestered and inactivated by DPP9 and bound CARD8-FL.

FIIND^{A} Alone Can Bind DPP9 and UPA^{B} Binding Is Not Released by VbP in Vitro

Modeling of the theoretical ZU5^{B} subdomain based on rigid superimposition of FIIND^{A} (containing both ZU5^{A} and UPA^{A}) onto UPA^{B} revealed steric clashes between ZU5^{B} and both DPP9 and FIIND^{A} (Figure 2A), confirming that molecule B of CARD8 represents autoproteolyzed and freed CT. To assess whether autoproteolysis was also required for molecule A binding, we solved the structure of autoproteolytic-deficient CARD8-S297A in complex with DPP9 (Figure S3, Table S1). The density of FIIND^{A} was similar to that in the ternary complex but UPA^{B} was entirely missing in this structure (Figure 2B), which confirms that each DPP9 monomer binds 1 molecule of FL-CARD8 (autoproteolyzed or not) and 1 molecule of already N-terminally degraded CARD8-CT.

The CARD8-CT binds adjacent to, but not inside of, the DPP9 substrate tunnel leading to the active site (Figure 2C–D). The DPP9 active site is known to undergo substantial rearrangement at a loop segment that folds into an α-helix, known as the R-helix, when R133 of the R-helix engages a substrate (Ross et al., 2018). Indeed, the R-helix is disordered in the CARD8-DPP9 complex (Figure 2C–D). This is directly in contrast to NLRP1, which buries the N-terminus of NLRP1-UPA^{B} into the DPP9 active site, resulting in R-helix ordering (Figure 2D) (Hollingsworth et al., 2020). The competitive DPP9 inhibitor VbP also causes R-helix ordering (Ross et al., 2018) and activates CARD8 (Johnson et al., 2018). To investigate whether inhibitor binding affected the UPA^{B} CARD8-CT, we solved the CARD8-DPP9-VbP structure at 3.3 Å resolution (Figure S4, Table S1). VbP bound directly into the DPP9 active site and resulted in R-helix ordering but did not displace either CARD8 molecule (Figure 2E–F, Figure S4G). This finding was again in direct contrast to human NLRP1, as VbP almost completely displaced NLRP1-UPA^{B} from DPP9 (Figure 2F) (Hollingsworth et al., 2020). Collectively, these findings rationalize the discrepancies observed in co-immunoprecipitation experiments between the human NLRP1-DPP9 complex and the CARD8-DPP9 complex (Griswold et al., 2019a; Zhong et al., 2018): human NLRP1-CT binds into the DPP9 active site and this interface is disrupted by inhibitors such as VbP, whereas CARD8-CT does not bind into the DPP9 active site and its binding is not directly affected by VbP.

Three Interfaces Mediate Ternary Complex Assembly

Like NLRP1, three large interfaces are involved in CARD8-DPP9 association: (I) ZU5^{A}-DPP9 (~950 Å^{2}/partner), (II) UPA^{B}-DPP9 (~600 Å^{2}/partner), and (III) UPA^{A}-UPA^{B} (800 Å^{2}/partner) (Figure 3A). Interface I is formed by β9 and the β4-β5 loop in ZU5^{A} and the WD40 domain of DPP9 (Figure S2B). Hydrophobic residues V277 and L278 in ZU5^{A} pack against L100, L101, L103 in DPP9 and K272-E274 in ZU5^{A} buries notable surface area by DPP9 association. Several notable hydrogen bonding interactions include M276 and E279 in ZU5^{A} between L102 and R96 in DPP9, respectively. Interface II involves interactions near the DPP9 active site tunnel including Y322 near the UPA^{B} N-terminus with DPP9's K43. Additionally, H39 in DPP9 wedges between T430 and E431 in UPA^{B} with hydrogen bonding interactions between both. Because the UPA^{B} N-terminus is disordered, interface II between CARD8 and DPP9 is far less extensive compared to interface II in the NLRP1-DPP9 complex. Interface III, on the other hand, is very similar to NLRP1 in that the sides of the UPA^{A} and UPA^{B} β-sandwich folds closely associate. Notably, F405/Y406 on

UPA^{A} (IIIa) and L368/F370 on UPA^{B} (IIIb) bury a marked amount of surface area through association (Figure 3A).

Structure-guided DPP9 mutations on interface I, in particular L100E/L101E (LL100EE) and L102E/L103E (LL102EE), and possibly R96E/K97E (RK96EE) and E597R, reduced the CARD8 interaction (Figure 3B) without affecting DPP9's catalytic activity (Hollingsworth et al., 2020). The K93E/K94E (KK93EE) mutation, however, may have affected DPP9's stability as shown by its lower expression. Addition of VbP during co-immunoprecipitation did not visibly reduce the DPP9-CARD8 interaction, underscoring the different binding modes of CARD8-UPA^{B} and VbP (Figure 3B). In summary, there are three distinct interfaces in the CARD8-DPP9 ternary complex and at least interface I is crucial for the ternary complex formation.

DPP9 Binding Restrains the CARD8 Inflammasome and UPA-UPA Interactions are Necessary for Inflammasome Signaling

We next generated structure-guided mutations on full-length CARD8 to assess the role of the ternary complex interfaces on inflammasome regulation. We managed to identify mutations on interface I (E274R of ZU5^{A}), IIIa (R394E and F405G of UPA^{A}), and IIIb (L368G and F370G of UPA^{B}) that preserved autoproteolysis as evidenced by the appearance of CARD8-CT in mutant and wild-type (WT) samples (Figure 3C). As expected, the interface I mutant abolished DPP9 binding. In contrast, interface III mutants maintained DPP9 binding (Figure 3C), likely due to the preserved interaction between full-length CARD8 and DPP9 at the A site. This explanation is supported by the ability of the autoprocessing-deficient CARD8-S297A mutant to pull down DPP9 at near WT amounts (Figure 3C), showing that the DPP9-CARD8^{A} interaction does not require CARD8^{B}. These data illustrate differences between NLRP1 and CARD8 in their assembly of DPP9-ternary complexes: for CARD8, FIIND^{A} can bind without an associated UPA^{B}. NLRP1, on the other hand, requires both copies for cooperative DPP9 association, and type III NLRP1 mutations impaired the FIIND^{A}-DPP9 interaction (Hollingsworth et al., 2020).

We could not obtain mutations on interface II that severely interfered with the CARD8-CT interaction with DPP9; these mutations either compromised protein expression or FIIND autoproteolysis, or had no effects. To elucidate if these mutational observations have a structural explanation, we performed further structural analysis on interfaces II and III of the CARD8-DPP9 vs NLRP1-DPP9 complexes (Table S2). Surface area burials on these interfaces in the CARD8-DPP9 complex are similar to those in the NLRP1-DPP9 complex (Hollingsworth et al., 2020). However, when we calculated the complex formation significance score (CSS) by the PISA server (Krissinel and Henrick, 2007) and the shape complementarity score (SC) by a CCP4 program (Winn et al., 2011), we found that while the interface II statistics of the two complexes are similar, interface III of the CARD8-DPP9 complex was predicted to be stronger with CSS of 1.0 and SC of 0.56, in comparison to CSS of 0.28 and CS of 0.51 for the NLRP1-DPP9 complex (Table S2). Thus, this analysis suggests that the more robust interface III likely necessitates very little if any association with DPP9's site II for ternary complex association, consistent with limited mutational effects on interface II. These data also provide an explanation for the observation that

CARD8 does not bind the DPP9 active site tunnel, whereas NLRP1 did, as the interface II interaction does not need to be conserved to cooperatively recruit CARD8-CT to DPP9.

We next assessed the functional impacts of these mutations by stably reconstituting *CARD8*$^{-/-}$ THP-1 cells (Johnson et al., 2018) with Tet-inducible *CARD8* constructs. For WT *CARD8*, the combination of doxycycline and VbP were required for cell death and gasdermin D (GSDMD) cleavage (Figure 3D). Doxycycline-induced expression of CARD8-E274R, an interface I mutant that cannot bind DPP9, caused pyroptosis in the absence of VbP with no significant increase upon its addition (Figure 3D). Thus, DPP9 binding restrains CARD8 inflammasome activation.

Despite maintaining FIIND autoprocessing, interface III mutations completely abolished inflammasome activity, even in the presence of the activating ligand VbP (Figure 3D). We reasoned that the observed UPA-UPA interface might be preserved on the inflammasome filament, as the UPA itself promotes CARD oligomerization and inflammasome activity (Qin et al., 2020; Hollingsworth et al., 2021). Additionally, NLRP1 interface III mutations abolished inflammasome signaling in cells (Hollingsworth et al., 2020) and disrupted filament formation in vitro (Huang et al., 2020). Consistent with this premise, only direct expression of the WT UPA-CARD, but not UPA-CARDs with interface III mutations nor the CARD alone, resulted in robust inflammasome signaling in a reconstituted HEK 293T system (Figure 3E).

DPP9 Requires FL-CARD8 to Sequester and Repress CARD8-CT

The above results indicate that CARD8-DPP9 binding is required to prevent the formation of an UPA-CARD inflammasome. We next asked whether FIIND^{A} was required to load CARD8-CT onto DPP9. We co-expressed CARD8-FIIND-S297A (FIIND-SA), which can only bind DPP9 site A, with CARD8-CT-FLAG, which can only bind DPP9 site B, in HEK 293T cells. FLAG immunoprecipitation indicated that CARD8-CT only captured DPP9 in the presence of FIIND-SA (Figure 4A), revealing that the CARD8-CT requires non-degraded FIIND^{A} for DPP9 association. These data are consistent with the reduction of both CARD8 and CARD8-CT interaction by structure-guided DPP9 mutations on interface I (Figure 3B). FIIND-SA with a site I mutation that abolishes DPP9 binding still associates with CARD8-CT (Figure 4A), indicating that CARD8 dimerization can occur in the absence of DPP9 through interface III. Mutations on interface III of FIIND-SA reduced its interaction with CARD8-CT as well as DPP9 (Figure 4A).

Since DPP9 association is required to repress CARD8 inflammasome activity and because CARD8-CT requires FIIND^{A} for DPP9 association, we postulated that CARD8-DPP9 ternary complex formation is required to repress CARD8-CT inflammasome activity. To test this hypothesis, we leveraged the degradation tag (dTAG) system, which facilitates controlled degradation of any FKBP12^{F36V} fusion protein in response to the ligand dTAG-13 (Nabet et al., 2018), to modulate the amount of free CARD8-CT. Briefly, when fused N-terminally to CARD8 (dTAG-CARD8-FL), dTAG-13 induces degradation of the CARD8-NT and liberates the free CARD8-CT due to FIIND autoprocessing (Figure 4B). Indeed, transient expression of dTAG-CARD8-FL in a reconstituted HEK 293T cell system caused marked cell death and GSDMD cleavage upon stimulation with dTAG-13 (Figure

4C). This pyroptotic phenotype was dependent on the amount of dTAG-CARD8-FL protein as well as the concentration of dTAG-13 (Figure 4C–D).

We next co-expressed increasing amounts of FIIND-SA along with dTAG-CARD8-FL in the reconstituted HEK 293T cell system (Figure 4E). Indeed, FIIND-SA rescued dTAG-13-induced cell death in a dose-dependent manner (Figure 4F). Additionally, interface I and III mutations abrogated FIIND-SA rescue (Figure 4G). The F405A interface IIIa mutant of FIIND-SA even failed to rescue a lower expressed dTAG-CARD8 (Figure 4G), providing stronger support for the defectiveness of these FIIND-SA mutants. Notably, the interface I mutant still preserved $FIIND^{A}$-UPA^{B} association through interface III (Figure 4A), demonstrating that DPP9 binding, and not CARD8 dimerization, represses the activity of CARD8-CT. Further, FIIND-SA from the homologous NLRP1 did not rescue dTAG-induced, CARD8-mediated cell death (Figure 4H). Thus, FL-CARD8, but not FL-NLRP1, recruits CARD8-CT to form the CARD8-DPP9 ternary complex, which ultimately represses CARD8 inflammasome formation.

VbP Activates CARD8 by N-terminal Degradation and Indirect Ternary Complex Disruption

We next evaluated the disruption of the NLRP1- and CARD8-ternary complexes by various DPP8/9 ligands *in vitro* (Figure 5A, S5). Although DPP9 binding restrains both NLRP1 and CARD8 inflammasome activation, VbP and the more selective DPP8/9 inhibitor 8j only directly disrupted the DPP9-NLRP1 ternary complex (Figure 5B, C), as expected. We next asked whether bulkier DPP8/9 ligands could displace the CARD8-CT from the ternary complex. We previously found that a fluorophosphonate (FP)-biotin activity-based probe with a long polyethylene glycol linker (Figure S5) that reacts with DPP8/9 active sites did not abolish the DPP9-CARD8 interaction (Griswold et al., 2019a). However, since FL-CARD8 can bind to the DPP9 A site without the CARD8-CT, this experiment did not actually evaluate the impact of FP-biotin on the ternary complex. Here, we instead expressed CARD8-S297A-FL with a C-terminal MYC tag together with CARD8-CT-FLAG before immunoprecipitating the ternary complex using anti-FLAG beads, thereby avoiding DPP9 pulldown as part of a binary complex with FL-CARD8. We found that the FP-biotin probe, unlike smaller DPP8/9 inhibitors, interfered with DPP9 capture by CARD8-CT (Figure 5D). Together, these data show that only large molecules that protrude from the DPP9 active site can directly displace CARD8-CT *in vitro*, further supporting our structural data.

We reasoned that it remained possible that DPP8/9 inhibition by VbP could nevertheless disrupt the CARD8 DPP9-ternary complex in cells, perhaps as an indirect consequence of inhibiting DPP8/9's catalytic activity. In order to test this hypothesis, we designed a HEK 293T system that decoupled N-terminal degradation from DPP9-ternary complex formation. We generated DPP9-ternary complexes with dTAG-CARD8-FL, which was completely degraded to release CARD8-CT in the presence of dTAG-13, and FIIND-SA, which lacks a disordered N-terminal segment required for VbP-stimulated N-terminal degradation (Chui et al., 2020) (Figure 5E). As expected, FIIND-SA repressed CARD8 activity. However, co-treatment with both dTAG-13 and VbP increased cell death and GSDMD processing compared to TAG-13 alone. To further increase confidence that this VbP-mediated effect was independent of additional dTAG-CARD8-FL degradation, we

generated a CARD8 dTAG-ZU5-UPA-CARD (dTAG-CARD8-ZUC) construct which lacks the N-terminal disordered region and is resistant to VbP induced N-terminal degradation and activation in HEK 293T cells (Figure 5F). Once again, VbP increased dTAG-13-dependent pyroptosis most noticeably in the presence of FIIND-SA.

Next, we stably expressed this CARD8 dTAG-ZUC construct in *CARD8*$^{-/-}$ THP-1 cells (Figure 5G). As expected, dTAG-13 induced rapid pyroptosis. Likewise, doxycycline-inducible CARD8-S297A-FL expression reduced sensitivity to dTAG-13, demonstrating that the DPP9-ternary complex can indeed repress CARD8 signaling in monocytes. Notably, VbP only synergized with dTAG-13 in the presence of FL-S297A. Together, these data indicate that VbP stimulation does indeed disrupt the DPP9-binding checkpoint in cells.

Based on our structure and *in vitro* experiments, we posited that VbP-induced ternary complex disruption is likely indirect and therefore reasoned it could only be observed in a cell-based system. To test this hypothesis, we ectopically expressed dTAG-CARD8-FL or dTAG-CARD8-ZUC with FLAG-tagged FIIND-SA in HEK 293T cells. The cells were then treated with dTAG-13 and/or VbP for 18 h prior to immunoprecipitation. dTAG-13 treatment induced degradation of dTAG-CARD8 and increased the amount of DPP9 captured by FIIND-SA-FLAG, indicating that the increased free CARD8-CT induced by dTAG-13 may enhance FIIND-SA-FLAG binding to DPP9 in cells (Figure 5G). Notably, VbP abrogated this increased binding indicating that the ternary complex stability is sensitive to VbP in cells despite such complexity not being fully reflected by *in vitro* systems (Figure 5H). As described below, we speculate that inhibition of DPP8/9's catalytic activity causes secondary effects on the DPP9-ternary complex in cells. Regardless, these data reveal that VbP activates the CARD8 inflammasome by two signals, induction of N-terminal degradation and disruption of the DPP9-ternary complex (Figure 5I).

DISCUSSION

In this study, we used a combination of structural, biochemical, and cell biological methods to dissect the molecular basis of CARD8 regulation by DPP9. Notably, CARD8 and NLRP1, which are related in their FIIND-mediated autoprocessing, DPP9-mediated suppression, and DPP8/9 inhibitor-mediated activation, share important similarities and differences. Both NLRP1 and CARD8 use a full-length FIIND and DPP9 (at site A) to capture a free CT containing the UPA subdomain of the FIIND (at site B), thereby forming a ternary complex that suppresses CT oligomerization and activation. However, the NLRP1-CT inserts into the DPP9 active site, but the CARD8-CT does not. This difference in binding modes may be explained by the N-terminal residues in NLRP1-CT, which possess a DPP9 substrate-like sequence (Ser-Pro); whereas the N-terminal residues in CARD8-CT are Ser-Leu. Furthermore, our structural analysis indicates a strong interaction between CARD8-FL and CARD8-CT through interface III, thus making interface II less important in the CARD8-DPP9 ternary complex. Due to this structural difference, the NLRP1-CT, but not the CARD8-CT, is directly displaced by DPP9 inhibitors *in vitro* (at site B), clarifying previously observed results. While also having a Ser-Pro sequence at the N-terminus of its CT, mouse NLRP1 does not appear to be displaced by VbP (Griswold et al., 2019a). Consistent with this observation, in the cryo-EM structure of the highly homologous rat

NLRP1 in complex with DPP9, the N-terminal residues of the CT insert into the DPP9 substrate channel but do not make specific interactions with the active site and the first few residues of the CT including the Ser-Pro sequence are disordered (Huang et al., 2020). Notably, neither human NLRP1 nor rodent NLRP1 are regulated by direct DPP9 cleavage (Griswold et al., 2019b; Hollingsworth et al., 2020).

Furthermore, despite lack of displacement of CARD8-CT from DPP9 by VbP *in vitro*, VbP treatment still reduced the association between DPP9 and CARD8-CT in cells and enhanced CARD8 inflammasome activation, suggesting that DPP9 inhibitors nevertheless impact CARD8 binding. We speculate that that DPP8/9 inhibition causes other cellular effects such as substrate accumulation to compete with CARD8 for DPP9 interaction. Indeed, we demonstrated that bulky molecules that protrude from the DPP9 active site could directly displace CARD8-CT. The mechanistic basis for this complex disruption in cells warrants further study.

In addition to these structural differences, CARD8 and NLRP1 exhibit distinct expression patterns, as noted above, and likely have different cellular functions. For example, CARD8 and NLRP1 may have evolved to respond to different pathogens. Consistent with this idea, recent reports revealed that human rhinovirus 3C protease and HIV protease directly cleave and activate human NLRP1 and CARD8, respectively (Robinson et al., 2020; Tsu et al., 2020; Wang et al., 2021). Moreover, human NLRP1 has also been recently reported to sense intracellular long double-stranded RNAs by directly binding them through its leucine-rich repeat (LRR) domain (Bauernfried et al., 2020), which is absent in CARD8. However, it should be noted that our studies suggest that CARD8 and NLRP1 may have also both evolved to sense a single endogenous danger signal triggered by DPP8/9 inhibition. Another important difference between CARD8 and NLRP1 is the structure of assembled inflammasome: while CARD8 can only directly recruit caspase-1 and activate rapid pyroptosis without causing cytokine maturation, NLRP1 recruits caspase-1 via ASC to elicit an inflammatory signaling cascade with cytokine secretion and pyroptotic cell death (Ball et al., 2020; Qin et al., 2020; Hollingsworth et al., 2021). In this context, it is possible that NLRP1 activation is more pro-inflammatory, as exemplified by the association of NLRP1 hyperactivation with a series of severe skin pro-inflammatory diseases (Drutman et al., 2019; Grandemange et al., 2017; Herlin et al., 2019; Jin et al., 2007; Levandowski et al., 2013; Soler et al., 2013; Zhong et al., 2016; Zhong et al., 2018). By contrast, CARD8 activation is more pro-death, shown by its ability to kill T cells and monocytic cancer cells without eliciting cytokine production (Johnson et al., 2020; Johnson et al., 2018; Linder et al., 2020; Okondo et al., 2016; Spagnuolo et al., 2013).

In summary, diverse pathogenic signals and the cellular consequence of DPP8/9 inhibition induce the N-terminal degradation of NLRP1 and CARD8, but this does not necessarily result in inflammasome formation. Instead, the freed CT is captured by a full-length NLRP1 or CARD8 together with DPP8/9, thereby preventing spurious inflammasome activation in cases with a low amount of N-terminal degradation. The fate of these ternary complexes remains unclear. While DPP9 itself does not directly degrade NLRP1-CT or CARD8-CT, we speculate other cellular machinery may recognize the ternary complex and destroy the sequestered CT fragment. If true, this would enable the DPP9-FL-CARD8 complex to

catalytically capture and eliminate CT. It is tempting to speculate that this ternary complex might also offer a second point of regulation, as signals that strengthen this interaction would enhance CARD8 or NLRP1 inhibition, while signals that weaken this interaction (e.g., DPP8/9 substrate buildup) would instead promote CARD8 or NLRP1 activation. As CARD8 and NLRP1 interact differently at the DPP9 active site channel, it is furthermore possible that these signals could impact CARD8 and NLRP1 in distinct ways. Both points of regulation point to homeostasis-altering molecular processes as cognate mechanisms to promote NLRP1 and CARD8 activation by diverse pathogenic and damage-associated molecular patterns upstream of inflammasome formation. However, more mechanistic studies are required to further address these questions.

LIMITATIONS OF STUDY

While we discovered that DPP9 sets a threshold for CARD8 inflammasome activation, the precise amount of CARD8 N-terminal degradation needed to overwhelm this checkpoint remains unstudied. Our results also demonstrated that while VbP does not directly compete with CARD8-CT for the DPP9 active site, cellular VbP treatment ultimately unleashes CARD8-CT in cells to activate the inflammasome. This mechanism warrants further study. Finally, CARD8-CTs must turnover to prevent their accumulation in cells, and this mechanism is presently unknown.

STAR★METHODS

CONTACT FOR REAGENT AND RESOURCE SHARING

Further information and requests for resources and reagents should be directed and will be fulfilled by the Lead Contact, Hao Wu (wu@crystal.harvard.edu). Study plasmids will be made available on Addgene (https://www.addgene.org/Hao_Wu/ and https://www.addgene.org/Daniel_Bachovchin/). Extended protocol are available on protocols.io (https://www.protocols.io/groups/hao-wu-lab). Pymol and chimera session files, in addition to other raw data, will be made available on our Open Science Framework (https://osf.io/x7dv8/). Cryo-EM data were deposited to EMPIAR, the EMDB, and the PDB.

EXPERIMENTAL MODEL AND SUBJECT DETAILS

HEK 293T Cell Lines—The human kidney epithelial cell line HEK 293T (ATCC) and related CASP1/GSDMD-expressing stable cell lines and *DPP8*$^{-/-}$, *DPP9*$^{-/-}$ lines were maintained in DMEM (GIBCO, ThermoFisher) supplemented with 10% fetal bovine serum (GIBCO, ThermoFisher Scientific), at 37°C, and 5% CO_2. HEK 293T cells were verified by the manufacturer. Cells were frequently checked for morphological features and tested for mycoplasma using MycoAlert Mycoplasma Detection kit (Lonza).

Expi293F Cell Line—Expi293F suspension cells were maintained in Expi293F Expression Medium (GIBCO, ThermoFisher) with constant shaking at 100 RPM, 37°C, 5% CO_2. Expi293F cells were not authenticated nor tested for mycoplasma contamination.

Sf9 Cell Line—Sf9 insect cells were maintained in HyClone SFX-Insect Cell Media (Cytiva) supplemented with 1X antibiotic-antimycotic (ThermoFisher) at 27°C with constant

shaking at 100 RPM. Sf9 cells were recently purchased from the manufacturer and were not authenticated.

THP-1 Cell Lines—THP-1 cells (ATCC) and related THP-1 *CARD8*$^{-/-}$ stable cell lines were grown in Roswell Park Memorial Institute (RPMI) medium 1640 with L-glutamine and 10% fetal bovine serum (GIBCO, ThermoFisher Scientific), at 37°C and 5% CO_2. Cells were monitored for morphological features and regularly tested for mycoplasma using MycoAlert Mycoplasma Detection kit (Lonza).

METHODS DETAILS

Constructs and Cloning—Full-length CARD8 (T60 isoform, Uniprot ID Q9Y2G2-5) was cloned into pcDNA3.1 LIC 6A (Addgene plasmid #30124) with a C-terminal FLAG tag and a modified pcDNA3.1 LIC 6D (Addgene plasmid #30127) construct (C-terminal TEV-GFP-FLAG tag). The short isoform of DPP9 (DPP9S, Uniprot ID Q86TI2-1) was also cloned into pcDNA3.1 LIC 6A (N-terminal FLAG-TEV tag or N-terminal His-TEV tag). CARD8 (with several synonymous mutations to avoid CRISPR/Cas9 editing) was also shuttled into pInducer20 vector (Addgene, #44012) using Gateway technology (Thermo Fischer Scientific) and pLEX_305-N-dTAG (Addgene, #91797). CARD8-ZUC containing the ZU5, UPA and CARD was cloned as previously described (Chui et al., 2020) and shuttled to pLEX_305-N-dTAG (Addgene, #91797). CARD8-CT constructs were synthesized (GenScript) with an N-terminal ubiquitin sequence followed by CARD8 (S297-L537), cloned into the pcDNA3.1 vector (Ub-CARD8-CT) and shuttled into the pLEX307 vector using Gateway technology (Thermo Fischer Scientific). Point mutations were introduced with Q5 site-directed mutagenesis (NEB) or QuikChange site-directed mutagenesis (Agilent). Most constructs will be made available on Addgene.

Cell Culture—HEK 293T cells and THP-1 cells were purchased from ATCC. HEK 293T cells were grown in Dulbecco's Modified Eagle's Medium (DMEM) with L-glutamine and 10% fetal bovine serum (FBS). THP-1 cells were grown in Roswell Park Memorial Institute (RPMI) medium 1640 with L-glutamine and 10% FBS. All cells were grown at 37° C in a 5% CO_2 atmosphere incubator. Cell lines were regularly tested for mycoplasma using the MycoAlert Mycoplasma Detection Kit (Lonza). THP-1 *CARD8*$^{-/-}$ cells and HEK 293T cells stably expressing caspase-1 and GSDMD were generated as previously described (Johnson et al., 2020). Reconstituted THP-1 *CARD8*$^{-/-}$ cells were generated via lentiviral infection of THP-1 *CARD8*$^{-/-}$ cells with the indicated pInducer20 construct followed by selection with G418 (Geneticin) at 200 μg/mL until all control cells were dead (approximately 14 days). dTAG-ZUC THP-1 cells were generated via lentiviral infection followed by selection with puromycin 500 ng/mL until all control cells were dead (approximately 7 days).

Protein Expression and Purification—To express CARD8-DPP9 complexes, Expi293F cells (1 L, 2–3 × 10^6 cells/mL) were co-transfected with CARD8-TEV-GFP-FLAG (0.7 mg) and DPP9S (0.3 mg) following incubation with polyethylenimine (3 mL, 1 mg/mL) in Opti-MEM (100 mL) for 30 min. 24 h later, cells were supplemented with glucose (9 mL, 45%) and valproic acid (10 mL, 300 mM). Cells were harvested 5 d after

transfection by centrifugation (2,000 RPM, 20 min), washed once with PBS, split into 3 pellets, flash-frozen in liquid nitrogen, and stored at −80 °C. Later, one thawed pellet was resuspended in lysis buffer (50–100 mL, 25 mM Tris-HCl pH 7.5, 150 mM NaCl, 1 mM TCEP), sonicated (2 s on 8 s off, 3.5 min total on, 40% power, Branson), and ultracentrifuged at 40,000 RPM for 1 h (45 Ti fixed-angle rotor, Beckman). The supernatant was incubated with pre-equilibrated (lysis buffer) anti-FLAG M2 affinity gel (Sigma, 1.0 mL) for 4 h at 4 °C, washed in batch once with lysis buffer (5 mL), and then washed by gravity flow with 25–50 column volumes (CV) lysis buffer. The CARD8-DPP9 complex was eluted by on-column cleavage at room temperature for 1 h using elution buffer (5 mL, 25 mM Tris-HCl pH 7.5, 150 mM NaCl, 1 mM TCEP, 0.2 mg TEV protease) and loaded onto a Mono Q 5/50 GL anion exchange column (Cytiva). Protein was eluted using a salt gradient from 150 mM to 1 M NaCl (25 mM Tris-HCl pH 8.0, 1 mM TCEP) over 15 CV. Mono Q eluent was concentrated using a 0.5 mL spin concentrator (Amicon Ultra, 50 kDa MW cutoff) to 0.5 mg/mL (assuming ε=1). Concentrated eluent was dialyzed overnight into EM buffer (25 mM HEPES pH 7.5, 150 mM NaCl, 1 mM TCEP) using a 0.5 mL Slide-A-Lyzer (ThermoFisher). Total protein yield varied between 2–3 mg per L of mammalian culture. Expression and purification of CARD8 (S297A) followed an identical protocol. Expression and purification of the VbP-bound complex followed an identical protocol except for the addition of 10 μM VbP to all purification and dialysis buffers.

Cryo-EM Screening and Data Collection—Grids were screened at University of Massachusetts Worcester, Pacific Northwest Center for Cryo-EM (PNCC), and Harvard Medical school (HMS) using a Talos Arctica microscope (ThermoFisher) operating at an acceleration voltage of 200 keV equipped with a direct electron detector. Small initial dataset collection revealed severe particle orientation preference for the CARD8-DPP9 maps, causing anisotropic resolution, in addition to dissociation of CARD8-DPP9 complexes. To remedy these issues, we crosslinked samples to avoid dissociation and tilted the stage to collect missing views (below).

The purified DPP9S-CARD8-WT or DPP9S-CARD8-S297A complex (0.40 mg/mL assuming ε=1; 25 mM HEPES pH 7.5, 150 mM NaCl, 1 mM TCEP, ±10 μM VbP) was crosslinked with 0.02% glutaraldehyde on ice for 5 min and immediately loaded onto a glow-discharged Quantifoil grid (R1.2/1.3 400-mesh gold-supported holey carbon, Electron Microscopy Sciences), blotted for 3–5 s under 100% humidity at 4 °C, and plunged into liquid ethane using a Mark IV Vitrobot (ThermoFisher). Grids were screened at Harvard Medical School for ice and particle quality prior to data collection. For data collection, movies were acquired at Harvard Medical School (DPP9-CARD8-WT) and National Center for CryoEM Access and Training (NCCAT) in New York (DPP9-CARD8-WT+VbP and DPP9-CARD8-S297A) using a Titan Krios microscope (ThermoFisher) at an acceleration voltage of 300 keV equipped with a BioQuantum K3 Imaging Filter (slit width 20 eV). Movies were recorded with a K3 Summit direct electron detector (Gatan) operating in counting mode at 105,000 × (0.825 Å/pix at HMS, 0.82 or 0.83 at Å/pix NCCAT).

For CARD8-DPP9 at 0° and 37°: 3,306 and 2,488 movies at a stage tilt of either 0° or 37° were collected using SerialEM (Mastronarde, 2005) at varying defocus values ranging between −0.8 to −2.2 μm and −1.5 to −3.0 μm, respectively. We used image shift to record

two shots for each of the four holes per stage movement. Movies were exposed with a total dose of 58.5 $e^{-}/Å^2$ for 2.22 s fractionated over 49 frames for 0° stage tilt movies and 64.99 $e^{-}/Å^2$ for 2.25 s fractionated over 49 frames for 37° stage tilt movies.

For CARD8-DPP9-VbP at 0° and 37°: 1,811 and 6,642 movies at a stage tilt of either 0° or 37°, respectively, were collected using Leginon (Suloway et al., 2005) at varying defocus values ranging between −1.1 to −3.4 μm. One shot was recorded for each of the four holes per stage movement through image shift. All movies were exposed with a total dose of 67.06 $e^{-}/Å^2$ for 1.5 s fractionated over 50 frames.

For CARD8(S297A)-DPP9, 3,840 movies were collected at a stage tilt of 37° using Leginon (Suloway et al., 2005) to vary the defocus range between −0.8 to −2.5 μm and to record one shot for each of the four holes per stage movement through image shift. All movies were exposed with a total dose of 63.67 $e^{-}/Å^2$ for 1.5 s fractionated over 50 frames.

Cryo-EM Data Processing—Data processing leveraged SBgrid Consortium (Morin et al., 2013) for support and computing resources. Movies collected at Harvard Medical School (CARD8-DPP9) were pre-processed on-the-fly by the facility's pipeline script. Movies were corrected by gain reference and for beam-induced motion and summed into motion-corrected images using the Relion 3.08 implementation of the MotionCor2 algorithm (Zheng et al., 2017). The CTFFIND4 program (Rohou and Grigorieff, 2015) was used to determine the defocus of each micrograph. Relion 3.1 (Scheres, 2012; Zivanov et al., 2018) was used for subsequent image processing. Movies collected at NCCAT (CARD8-DPP9-VbP) were similarly pre-processed using Relion 3.1.

For the CARD8-DPP9 complex, template-free autopicking with crYOLO (Wagner et al., 2019) (generalized training for on-the-fly picking at the HMS cryo-EM center) selected 487,952 particles from 3,306 micrographs, which were subjected to a single round of 2D classification. The heterogenous nature of the sample was evident in 2D class averages because complexes containing only DPP9, 2CARD8:2DPP9, and 4CARD8:2DPP9 were present. A randomized set of 100,000 particles was selected for the *de novo* reconstruction of an initial model, which was low-pass-filtered to 40 Å to use as the input reference for 3D classification. Multiple rounds of 3D classification including global and local fine angular search were performed. After visual inspection, one class with 2CARD8:2DPP9 (62,018 particles) was selected for 3D refinement. Subsequently, particles were CTF refined and Bayesian polished to reach an overall resolution of 3.3 Å. However, the map suffered from anisotropic resolution, and cryoEF (Naydenova and Russo, 2017) analysis estimated that data collected at a tilt angle of 37° was ideal to fill the gaps in Fourier space.

The overall processing scheme for tilt data was derived from the work flow of tilt dataset described in Zivanov *et al.* 2018 (Zivanov et al., 2018). For CARD8-DPP9 data collected at a 37° tilt, micrographs were first motion-corrected with MotionCor2 (Zheng et al., 2017) followed by Gctf (Zhang, 2016) to calculate per micrograph defocus values in Relion 3.1. Template-free autopicking with crYOLO (Wagner et al., 2019) then picked 313,425 particles from 2,488 micrographs. After multiple rounds of 2D classification, 243,459 visually homogenous particles remained for further processing. A random subset comprising

121,730 of these particles was used for *de novo* initial model construction, which was then low-passed filtered (30 Å) and used as the initial reference map for 3D classification. After one round of 3D classification, a 3D class with 58,980 particles was selected for high-resolution refinement. The first 3D refinement using these particles yielded a 5.2 Å resolution structure and the Fourier shell correlation (FSC) curve showed strong fluctuations indicating imprecisions in CTF estimation. We then utilized CTF refinement implemented in Relion 3.1, including higher order aberrations correction, anisotropic magnification corrections, and per-particle defocus estimation (Zivanov et al., 2020). Iterative rounds of 3D refinement followed by CTF refinement and Bayesian polishing gradually improved the resolution and this iterative process was stopped when we observed a resolution plateau at 3.8 Å. Refined and polished particle sets from 0° and 37° stage-tilt data were merged and 3D refinement was performed. The merged data was then reconstructed to give an overall resolution of 3.3 Å as calculated by gold-standard FSC between half maps, with much improved CARD8 density (Figure S1).

For the CARD8-DPP9-VbP complex, template-free autopicking with crYOLO (Wagner et al., 2019) (trained with 10 manually-picked high-contrast micrographs) yielded 1,404,573 particles from 1,811 micrographs that were collected without stage tilt. These particles were subjected to multiple rounds of 2D classification that yielded visually homogeneous 2D classes with 471,255 particles. A randomized set of 100,000 particles was selected for the *de novo* reconstruction of an initial model, which was low-pass-filtered to 30 Å to use as the input reference for 3D classification. Multiple rounds of 3D classification including global and local fine angular search were performed. After visual inspection, one 3D class (89,909 particles) was selected for 3D refinement. Subsequently, particles were CTF refined and Bayesian polished to reach an overall resolution of 3.5 Å. However, the map suffered from anisotropic resolution, and cryoEF (Naydenova and Russo, 2017) analysis estimated that data collected at a tilt angle of 37° degrees was ideal to fill the gaps in Fourier space (below).

The overall processing scheme for tilt data analysis of CARD8-DPP9-VbP was derived from CARD8-DPP9 data processing (described above). Briefly, micrographs were first motion-corrected with MotionCor2 (Zheng et al., 2017) followed by Gctf (Zhang, 2016) to calculate per micrograph defocus values in Relion 3.1. Template-free autopicking with crYOLO (Wagner et al., 2019) then picked 1,889,993 particles from 6642 micrographs. After multiple rounds of 2D classification, 840,902 visually homogenous particles remained for further processing. A random subset comprising 100,000 of these particles was used for *de novo* initial model construction, which was then low-passed filtered (30 Å) and used as the initial reference map for 3D classification. After multiple rounds of 3D classification, a 3D class with 91,254 particles was selected for high-resolution refinement. The first 3D refinement using these particles yielded a 5.8 Å resolution structure, and the FSC curve showed strong fluctuations indicating imprecisions in CTF estimation. We then utilized CTF refinement implemented in Relion 3.1, including correction for higher order aberrations and anisotropic magnification, and per-particle defocus estimation (Zivanov et al., 2020). Iterative rounds of 3D refinement followed by CTF refinement and Bayesian polishing gradually improved the resolution and this iterative process was stopped when we observed a resolution plateau at 3.4 Å. Refined particle sets from 0° and 37° stage-tilt data were

merged and 3D refinement was performed. The merged data was then 3D classified with fine local search angles to give a final stack of 146,101 particles which was reconstructed to give an overall resolution of 3.3 Å as calculated by gold-standard FSC between half maps, with much improved CARD8 density (Figure S4).

The DPP9-CARD8-S297A complex was processed in cryoSPARC (Punjani et al., 2017). 3,840 movies collected at 37° stage tilt were summed into motion-corrected micrographs with Patch-Motion in cryoSPARC (Punjani et al., 2017). Next, defocus values were determined with cryoSPARC's Patch-CTF function (Punjani et al., 2017). 5,505,288 particles were picked by blob picking and the 2D classes following two rounds of classification were used as input to re-pick 1,634,615 particles. Following 3 rounds of 2D classification, 191,609 particles remained and were used to generate 3 ab-initio models. At this stage, heterogeneity between bound and unbound DPP9 particles was evident, and a round of heterogeneous refinement (2 classes) yielded a reconstruction from 92,404 particles at a nominal resolution of 4.88 Å. These particles were used for a final round of non-uniform refinement (Punjani et al., 2019) which converged at an overall resolution of 3.86 Å as calculated by gold-standard FSC (Figure S3).

Atomic Model Building—The cryo-EM maps were first fit with the crystal structure of DPP9 dimer (PDB ID: 6EOQ) (Ross et al., 2018). A homology model of CARD8-FIIND was generated with Schrodinger Prime (Jacobson et al., 2002) using the structure of NLRP1-FIIND (Qin et al., 2020; Robert Hollingsworth et al., 2021) as template. Manual adjustment and *de novo* building of missing segments, rigid-body fitting, flexible fitting, and segment-based real-space refinement were performed in distinct parts of the initial model to fit in the density in Coot (Emsley et al., 2010), with help of UCSF-Chimera (Goddard et al., 2007) and real-space refinement in Phenix (Klaholz, 2019). A few unstructured regions, including parts of the UPA, were omitted owing to poor density. The full model represents Asp18-Met1356 amino acids of DPP9 (short isoform, Uniprot ID Q86TI2-1), $ZU5^{A}$ Gly166-Ser295, UPA^{A} Arg304-Pro446 and UPA^{B} Leu320-Pro446 of CARD8 (isoform 5, Uniprot ID Q9Y2G2-5).

For the VbP-bound structure, the full model represents Asp18-Leu863 amino acids of DPP9 (short isoform, Uniprot ID Q86TI2-1), $ZU5^{A}$ Gly166-Ser295, UPA^{A} Arg304-Pro445 and UPA^{B} Leu320-Pro446 of CARD8 (isoform 5, Uniprot ID Q9Y2G2-5). We modelled covalently linked DPP9 S730-VbP in the cryo-EM map density using NLRP1-DPP9-VbP (PDB ID: 6X6C) and DPP8-VbP (PDB ID: 6HP8) (Díaz, 2018) as templates. DPP9-VbP interactions are similar to those observed in the DPP8-VbP complex in addition to DPPIV bound to substrate (PDB ID: 5YP3) (Roppongi et al., 2018) (Figure S4G).

For both structures, interaction analysis was conducted visually and using PISA (Krissinel and Henrick, 2007). Structure representations were generated in ChimeraX (Goddard et al., 2018), Pymol, and ResMap (Kucukelbir et al., 2014). Ligand interaction analysis was conducted with Maestro (Schrödinger Release 2020-1, 2020). Pymol and ChimeraX session files are available on our Open Science Framework repository (https://osf.io/x7dv8/). Schematics were created with BioRender.

Negative Stain Electron Microscopy—Copper grids coated with layers of plastic and thin carbon film (Electron Microscopy Sciences) were glow discharged before 4 μl of purified proteins were applied. Samples were left on the grids for 45 sec, blotted, and then stained with 1% uranyl formate for 40 s, blotted, and air dried. The grids were imaged on a JEOL 1200EX or Tecnai G^2 Spirit BioTWIN microscope at the HMS EM facility operating at 80 keV.

Immunoblotting.—Samples were run on either NuPAGE™ 4 to 12%, Bis-Tris 1.0 mm, Mini Protein Gel (Invitrogen) for 30 min at 175 V or NuPAGE™ 4 to 12%, Bis-Tris, 1.0 mm, Midi Protein Gel (Invitrogen) for 45–60 min at 175 V. Gels were transferred to nitrocellulose with the Trans-Blot Turbo Transfer System (BIO-RAD). Membranes were blocked with Intercept™ (TBS) Blocking Buffer (LI-COR) for 30 min at ambient room temperature, prior to incubating with primary antibody (1:1,000 in Intercept™ Blocking Buffer) overnight at 4 °C. Blots were washed 3 times with TBST buffer prior to incubating with secondary antibody (1:10,000 in Intercept™ Blocking Buffer) for 60 min at ambient room temperature. Blots were washed 3 times with TBST buffer, rinsed with water and imaged via Odyssey CLx (LI-COR).

Immunoprecipitation Assays—For DPP9 mutants (Figure 3B), *DPP8*$^{-/-}$, *DPP9*$^{-/-}$ HEK 293T cells (Hollingsworth et al., 2020) were seeded at 1×10^6 cells/well in 6-well tissue culture dishes. The following day cells were transfected with plasmids encoding for CARD8 (2 μg) or the indicated FLAG-tagged DPP9 construct (2 μg) with FuGENE HD according to manufacturer's instructions (Promega). Cells were harvested and washed 3x with PBS. Pellets were lysed in Tris-Buffered Saline (TBS) with 0.5% NP-40 using pulse sonication and centrifuged at 20,000 × *g* for 10 min at 4 °C. DPP9 and CARD8 lysates were mixed in a 1:1 ratio prior to treating with DMSO or VbP (10 μM) for 1 h. They were incubated with 20 μL of anti-FLAG-M2 agarose resin (Sigma) overnight at 4 °C. After washing 3 × 500 μL with cold PBS in microcentrifuge spin columns (Pierce), bound proteins were eluted by incubating resin with 40 μL of PBS with 150 ng/μL 3x-FLAG peptide for 1 h at 4 °C. An equal volume of 2x sample loading was added to the eluate and boiled. Protein content was evaluated by immunoblotting with the following antibodies: DPP9 rabbit polyclonal Ab (Abcam, Ab42080), FLAG® M2 monoclonal Ab (Sigma, F3165), CARD8 C terminus rabbit polyclonal Ab (Abcam, ab24186), and GAPDH rabbit polyclonal Ab (CST, 14C10).

For CARD8 mutants (Figure 3C), HEK 293T cells were seeded at 0.5×10^6 cells/well in 6-well tissue culture dishes. The following day cells were transfected with plasmids encoding for the indicated FLAG-tagged CARD8 construct (2 μg) with FuGENE HD according to manufacturer's instructions (Promega). Cells were harvested and washed 3x with PBS. Pellets were lysed in Tris-Buffered Saline (TBS) with 0.5% NP-40 using pulse sonication and centrifuged at 20,000 × *g* for 10 min at 4 °C. The clarified lysates were normalized by DC protein assay (BIO-RAD) and incubated with 20 μL of anti-FLAG-M2 agarose resin (Sigma) overnight at 4 °C. After washing 3 × 500 μL with cold PBS, bound proteins were eluted by incubating resin with 40 μL of PBS with 150 ng/μL 3x-FLAG peptide for 1 h at 4 °C. An equal volume of 2x sample loading was added to the eluate and boiled. Protein content was evaluated by immunoblotting with the following antibodies: DPP9

rabbit polyclonal Ab (Abcam, Ab42080), FLAG® M2 monoclonal Ab (Sigma, F3165), and GAPDH rabbit polyclonal Ab (CST, 14C10).

For ternary complex capture experiments (Figure 4A), HEK 293T cells were seeded at 5×10^5 cells/well in 6-well tissue culture dishes. The following day the cells were transfected with plasmids encoding for FLAG-tagged CARD8-CT (1 μg), the indicated MYC-tagged CARD8-FIIND-SA (1 μg), and RFP (to 2 μg) with FuGENE HD according to manufacturer's instructions (Promega). After 48 h cells were harvested and washed 3x with PBS. Pellets were lysed in Tris-Buffered Saline (TBS) with 0.5% NP-40 using pulse sonication and centrifuged at 20,000 × *g* for 10 min at 4 °C. Lysates were incubated with 20 μL of anti-FLAG-M2 agarose resin (Sigma) overnight at 4 °C. After washing 3 × 500 μL with cold PBS in microcentrifuge spin columns (Pierce), bound proteins were eluted by incubating resin with 40 μL of PBS with 150 ng/μL 3x-FLAG peptide for 1 h at 4 °C. An equal volume of 2x sample loading was added to the eluate and boiled. Protein content was evaluated by immunoblotting with the following antibodies: DPP9 rabbit polyclonal Ab (Abcam, Ab42080), FLAG® M2 monoclonal Ab (Sigma, F3165), Myc-tag (71D10) rabbit monoclonal Ab (CST, #2278), and GAPDH rabbit polyclonal Ab (CST, 14C10).

For on-bead displacement experiments (Figure 5A–C), HEK 293T cells were seeded at 3×10^6 cells in a 10 cm tissue culture dish. The following day the cells were transfected with plasmids encoding for FLAG-tagged DPP9 (2 μg), V5-tagged Ub-S297 CARD8 or V5-tagged Ub-S1213 NLRP1 (3 μg), and MYC-tagged CARD8 S297A or MYC-tagged NLRP1 S1213A (5 μg) with FuGENE HD according to manufacturer's instructions (Promega). Cells were harvested and washed 3x with PBS. Pellets were lysed in Tris-Buffered Saline (TBS) with 0.5% NP-40 using pulse sonication and centrifuged at 20,000 × *g* for 10 min at 4 °C. Lysates were incubated with 100 μL of anti-FLAG-M2 agarose resin (Sigma) for 2 h at 4 °C. The agarose was washed once with PBS, and subsequently split into 4 × 25 μL aliquots. 50 μL of PBS containing DMSO, VbP (10 μM), 8J (50 μM), Bestatin methyl ester (MeBS, 10 μM) at RT for 1 h in microcentrifuge spin columns (Pierce). Displaced proteins were collected via centrifugation. The resin was washed 3x with cold PBS, followed by elution with 3x-FLAG peptide as above. Protein content was evaluated by immunoblotting with the following antibodies: FLAG® M2 monoclonal Ab (Sigma, F3165), Myc-tag (71D10) rabbit monoclonal Ab (CST, #2278), and V5 rabbit polyclonal Ab (Abcam, ab9116).

For FP-biotin displacement experiments (Figure 5D), HEK 293T cells were seeded at 3×10^6 cells in a 10 cm tissue culture dish. The following day the cells were transfected with plasmids encoding for MYC-tagged CARD8-S297A-FL (10 μg) or FLAG-tagged Ub-S297 CARD8 (10 μg) with FuGENE HD according to manufacturer's instructions (Promega). Cells were harvested and washed 3x with PBS. Pellets were lysed in Tris-Buffered Saline (TBS) with 0.5% NP-40 using pulse sonication, mixed and centrifuged at 20,000 × *g* for 10 min at 4 °C. Lysates were split into 3 aliquots and incubated with DMSO, VbP (10 μM) or FP PEG23 biotin (10 μM) at room ambient temperature for 1 h. Lysates were incubated with 20 μL of anti-FLAG-M2 agarose resin (Sigma) overnight at 4 °C. After washing 3 × 500 μL with cold PBS in microcentrifuge spin columns (Pierce), bound proteins were eluted by incubating resin with 40 μL of PBS with 150 ng/μL 3x-FLAG peptide for 1 h at 4 °C. An equal volume of 2x sample loading was added to the eluate and boiled. Protein content

was evaluated by immunoblotting with the following antibodies: DPP9 rabbit polyclonal Ab (Abcam, Ab42080), FLAG® M2 monoclonal Ab (Sigma, F3165), Myc-tag (71D10) rabbit monoclonal Ab (CST, #2278), IRDye 600 RD streptavidin (LI-COR, 926-68079) and GAPDH rabbit polyclonal Ab (CST, 14C10).

For dTAG ternary complex experiments (Figure 5H), HEK 293T cells were seeded at 5×10^5 cells/well in 6-well tissue culture dishes. The following day the cells were transfected with plasmids encoding for FLAG-tagged CARD8-FIIND-S297A (1 μg), and dTAG-CARD8 (1 μg). The next day cells were treated with dTAG-13 (500 nM) and VbP (10 μM) for 24 h prior to harvesting. Anti-FLAG immunoprecipitation was executed as described above. Protein content was evaluated by immunoblotting with the following antibodies: FLAG® M2 monoclonal Ab (Sigma, F3165), HA-Tag (C29F4) rabbit monoclonal (CST, #3724), DPP9 rabbit polyclonal Ab (Abcam, Ab42080), and GAPDH rabbit polyclonal Ab (CST, 14C10).

LDH Cytotoxicity Assay—For THP-1 *CARD8*$^{-/-}$ cells stably expressing the indicated pInducer20 CARD8 construct (Figure 3D), cells were seeded at 2.5×10^5 cells/mL in 12-well tissue culture dishes. The cells were treated with the indicated combination of doxycycline (1 μg/mL) and VbP (10 μg/mL) for 24 h. For HEK 293T cells stably expressing CASP-1 and GSDMD-V5 (Figure 3E), cells were seeded at 1.5×10^5 cells/mL in 12-well tissue culture dishes. The following day the cells were transfected with plasmids encoding for the indicated CARD8-CT construct (0.1 μg) and RFP as a filler vector (to 2 μg) per 125 μL of Opti-MEM with FuGENE HD according to manufacturer's instructions (Promega).

In all cases, supernatants were analyzed for LDH activity using the CyQUANT™ LDH Cytotoxicity Assay Kit (ThermoFisher) and lysates protein content was evaluated by immunoblotting with a combination of the following antibodies: CARD8 CT rabbit polyclonal Ab (Abcam, Ab24186), CASP1 rabbit polyclonal Ab (CST, #2225), GSDMDC1 rabbit polyclonal Ab (Novus, NBP2-33422), HA-Tag (C29F4) rabbit monoclonal (CST, #3724) and GAPDH rabbit polyclonal Ab (CST, 14C10).

dTAG Assays—HEK 293T cells stably expressing CASP-1 and GSDMD-V5 (Figure 4C–D, F–H and Figure 5D–E) were seeded at 1.5×10^5 cells/mL in 12-well tissue culture dishes. The following day the cells were transfected with plasmids encoding for the indicated amount of plasmids encoding for dTAG-CARD8 or dTAG-CARD8 ZUC and CARD8 FIIND-S297A or NLRP1 FIIND-S1213A constructs with RFP as a filler vector (to 2 μg) per 125 μL of Opti-MEM with FuGENE HD according to manufacturer's instructions (Promega). After 24 h (dTAG-CARD8) or 48 h (dTAG-CARD8 ZUC) cells were treated with DMSO, dTAG-13 (500 nM, unless otherwise indicated), and/or VbP (10 μM) for 3h prior to harvesting for analysis of supernatants for LDH release and lysates for protein content as detailed above (see Immunoblotting).

THP-1 *CARD8*$^{-/-}$ cells stably expressing dTAG-CARD8 ZUC (Figure 5F) were seeded at 2×10^5 cells/mL in 12-well tissue culture dishes. Cells were treated with doxycycline (1 μg/mL) for 48h followed by dTAG-13 (5 nM) and VbP (10 μM) for 3h prior to harvesting

for analysis of supernatants for LDH release as detailed above (see LDH Cytotoxicity Assay).

QUANTIFICATION AND STATISTICAL ANALYSIS

Statistical significance was calculated by using GraphPad Prism version 7, GraphPad Software, San Diego, California USA, www.graphpad.com. The number of independent experiments, the statistical significance, and the statistical test used to determine the significance are indicated in each figure or figure legend or method section where quantification is reported.

DATA AVAILABILITY

The cryo-EM maps have been deposited in the Electron Microscopy Data Bank under the accession numbers EMD-22367 (CARD8-DPP9), EMD-22402 (CARD8-DPP9-VbP), and EMD-22974 (CARD8-S297A-DPP9). The atomic coordinates have been deposited in the Protein Data Bank under the accession numbers PDB ID 7JKQ (CARD8-DPP9) and PDB ID 7JN7 (CARD8-DPP9-VbP). Raw cryo-EM data have been deposited into EMPIAR under the accession numbers EMPIAR-10597 (CARD8-DPP9), EMPIAR-10596 (CARD8-DPP9-VbP), and EMPIAR-10600 (CARD8-S297A-DPP9). Extended protein purification protocols will be made available on Protocols.io (https://www.protocols.io/groups/hao-wu-lab). Pymol session files and full-sized figures will be made available on OSF (https://osf.io/x7dv8/). Most constructs will be made available on Addgene. All other data and materials can be obtained from the corresponding authors upon reasonable request.

Supplementary Material

Refer to Web version on PubMed Central for supplementary material.

ACKNOWLEDGEMENTS

We thank T.-M. Fu of the laboratory of H.W. for initiating a CARD8 alone project, all members of the laboratories of H.W. and D.A.B. for helpful discussions, Dr. Maria Ericsson at the HMS EM facility for advice and training, and Drs. Richard Walsh, Sarah Sterling, and Shaun Rawson at the Harvard Cryo-EM Center for Structural Biology for cryo-EM training and productive consultation. We thank Drs. Kangkang Song and Kyounghwan Lee for data collection at UMass Medical School. We thank Daija Bobe and Dr. Ed Eng for data collection at the National Center for CryoEM Access and Training (NCCAT) and the Simons Electron Microscopy Center located at the New York Structural Biology Center, supported by the NIH Common Fund Transformative High Resolution Cryo-Electron Microscopy program (U24 GM129539,) and by grants from the Simons Foundation (SF349247) and NY State. We thank Theo Humphreys and the Pacific Northwest Center for Cryo-EM (PNCC) at Oregon Health & Science University for screening and preliminary dataset collection, under the NIH grant U24GM129547 and accessed through EMSL (grid.436923.9), a DOE Office of Science User Facility sponsored by the Office of Biological and Environmental Research. We also thank Drs. Irina Novikova, Harry Scott, and Craig Yoshioka at PNCC for cryo-EM data processing training. pInducer20 was a gift from Stephen Elledge (Addgene plasmid # 44012). pLEX_307 was a gift from David Root (Addgene plasmid # 41392). pcDNA3.1 LIC 6A and pcDNA 3.1 LIC 6D were gifts from Scott Gradia (Addgene plasmid #30124 and #30127). pLEX_305-N-dTAG was a gift from James Bradner & Behnam Nabet (Addgene plasmid #91797) This work was supported by National Institutes of Health grants DP1 HD087988 and R01 AI124491 to H.W., T32-GM007726 and F31-AI152267-01A1 to L.R.H., T32 GM007739-Andersen and F30 CA243444 to A.R.G., the Memorial Sloan Kettering Cancer Center Core Grant P30 CA008748 and R01 AI137168 to D.A.B. We thank BioRender for figure design and SBGrid for computing support.

REFERENCES

Bagnall RD, Roberts RG, Mirza MM, Torigoe T, Prescott NJ, and Mathew CG (2008). Novel isoforms of the CARD8 (TUCAN) gene evade a nonsense mutation. European Journal of Human Genetics 16, 619–625. [PubMed: 18212821]

Ball DP, Taabazuing CY, Griswold AR, Orth EL, Rao SD, Kotliar IB, Vostal LE, Johnson DC, and Bachovchin DA (2020). Caspase-1 interdomain linker cleavage is required for pyroptosis. Life Sci Alliance 3, e202000664. [PubMed: 32051255]

Bauernfried S, Scherr MJ, Pichlmair A, Duderstadt KE, and Hornung V (2020). Human NLRP1 is a sensor for double-stranded RNA. Science, eabd0811. [PubMed: 33243852]

Broz P, and Dixit VMInflammasomes: mechanism of assembly, regulation and signalling. Nat Rev Immunol.

Chui AJ, Griswold AR, Taabazuing CY, Orth EL, Gai K, Rao SD, Ball DP, Hsiao JC, and Bachovchin DA (2020). Activation of the CARD8 Inflammasome Requires a Disordered Region. Cell Reports 33, 108264. [PubMed: 33053349]

Chui AJ, Okondo MC, Rao SD, Gai K, Griswold AR, Johnson DC, Ball DP, Taabazuing CY, Orth EL, Vittimberga BA, et al. (2019). N-terminal degradation activates the NLRP1B inflammasome. Science 364, 82–85. [PubMed: 30872531]

D'Osualdo A, Weichenberger CX, Wagner RN, Godzik A, Wooley J, and Reed JC (2011). CARD8 and NLRP1 Undergo Autoproteolytic Processing through a ZU5-Like Domain. PLoS One 6, e27396. [PubMed: 22087307]

Díaz BHR (2018). Improvement of Protein Crystal Diffraction Using Post-Crystallization Methods: Infrared Laser Radiation Controls Crystal Order In Fachbereich Physik (Hamburg: Universität Hamburg).

Drutman SB, Haerynck F, Zhong FL, Hum D, Hernandez NJ, Belkaya S, Rapaport F, de Jong SJ, Creytens D, Tavernier SJ, et al. (2019). Homozygous NLRP1 gain-of-function mutation in siblings with a syndromic form of recurrent respiratory papillomatosis. Proc Natl Acad Sci U S A 116, 19055–19063. [PubMed: 31484767]

Emsley P, Lohkamp B, Scott WG, and Cowtan K (2010). Features and development of Coot. Acta Crystallogr D 66, 486–501. [PubMed: 20383002]

Finger JN, Lich JD, Dare LC, Cook MN, Brown KK, Duraiswami C, Bertin JJ, and Gough PJ (2012). Autolytic Proteolysis within the Function to Find Domain (FIIND) Is Required for NLRP1 Inflammasome Activity. J Biol Chem 287, 25030–25037. [PubMed: 22665479]

Goddard TD, Huang CC, and Ferrin TE (2007). Visualizing density maps with UCSF Chimera. J Struct Biol 157, 281–287. [PubMed: 16963278]

Goddard TD, Huang CC, Meng EC, Pettersen EF, Couch GS, Morris JH, and Ferrin TE (2018). UCSF ChimeraX: Meeting modern challenges in visualization and analysis. Protein Science 27, 14–25. [PubMed: 28710774]

Grandemange S, Sanchez E, Louis-Plence P, Tran Mau-Them F, Bessis D, Coubes C, Frouin E, Seyger M, Girard M, Puechberty J, et al. (2017). A new autoinflammatory and autoimmune syndrome associated with NLRP1 mutations: NAIAD (NLRP1-associated autoinflammation with arthritis and dyskeratosis). Annals of the rheumatic diseases 76, 1191–1198. [PubMed: 27965258]

Griswold AR, Ball DP, Bhattacharjee A, Chui AJ, Rao SD, Taabazuing CY, and Bachovchin DA (2019a). DPP9's Enzymatic Activity and Not Its Binding to CARD8 Inhibits Inflammasome Activation. ACS Chem Biol 14, 2424–2429. [PubMed: 31525884]

Griswold AR, Cifani P, Rao SD, Axelrod AJ, Miele MM, Hendrickson RC, Kentsis A, and Bachovchin DA (2019b). A Chemical Strategy for Protease Substrate Profiling. Cell Chem Biol 26, 901–907 e906. [PubMed: 31006619]

Herlin T, Jørgensen SE, Høst C, Mitchell PS, Christensen MH, Laustsen M, Larsen DA, Schmidt FI, Christiansen M, and Mogensen TH (2019). Autoinflammatory disease with corneal and mucosal dyskeratosis caused by a novel NLRP1 variant. Rheumatology.

Hollingsworth LR, Sharif H, Griswold AR, Fontana P, Mintseris J, Dagbay KB, Paulo JA, Gygi SP, Bachovchin DA, and Wu H (2020). DPP9 directly sequesters the NLRP1 C-terminus to repress inflammasome activation. bioRxiv, 2020.2008.2014.246132.

Huang M, Zhang X, Ann TG, Gong Q, Wang J, Han Z, Wu B, Zhong F, and Chai J (2020). Structural and biochemical mechanisms of NLRP1 inhibition by DPP9. bioRxiv, 2020.2008.2013.250241.

Jacobson MP, Friesner RA, Xiang Z, and Honig B (2002). On the Role of the Crystal Environment in Determining Protein Side-chain Conformations. J Mol Biol 320, 597–608. [PubMed: 12096912]

Jin Y, Mailloux CM, Gowan K, Riccardi SL, LaBerge G, Bennett DC, Fain PR, and Spritz RA (2007). NALP1 in vitiligo-associated multiple autoimmune disease. N Engl J Med 356, 1216–1225. [PubMed: 17377159]

Johnson DC, Okondo MC, Orth EL, Rao SD, Huang H-C, Ball DP, and Bachovchin DA (2020). DPP8/9 inhibitors activate the CARD8 inflammasome in resting lymphocytes. Cell Death & Disease 11, 628. [PubMed: 32796818]

Johnson DC, Taabazuing CY, Okondo MC, Chui AJ, Rao SD, Brown FC, Reed C, Peguero E, de Stanchina E, Kentsis A, et al. (2018). DPP8/DPP9 inhibitor-induced pyroptosis for treatment of acute myeloid leukemia. Nature medicine 24, 1151–1156.

Klaholz B (2019). Deriving and refining atomic models in crystallography and cryo-EM: the latest Phenix tools to facilitate structure analysis. Acta Crystallographica Section D 75, 878–881.

Krissinel E, and Henrick K (2007). Inference of macromolecular assemblies from crystalline state. Journal of molecular biology 372, 774–797. [PubMed: 17681537]

Kucukelbir A, Sigworth FJ, and Tagare HD (2014). Quantifying the local resolution of cryo-EM density maps. Nat Methods 11, 63–65. [PubMed: 24213166]

Larkin MA, Blackshields G, Brown NP, Chenna R, McGettigan PA, McWilliam H, Valentin F, Wallace IM, Wilm A, Lopez R, et al. (2007). Clustal W and Clustal X version 2.0. Bioinformatics 23, 2947–2948. [PubMed: 17846036]

Levandowski CB, Mailloux CM, Ferrara TM, Gowan K, Ben S, Jin Y, McFann KK, Holland PJ, Fain PR, Dinarello CA, et al. (2013). NLRP1 haplotypes associated with vitiligo and autoimmunity increase interleukin-1β processing via the NLRP1 inflammasome. Proc Natl Acad Sci USA 110, 2952–2956. [PubMed: 23382179]

Linder A, Bauernfried S, Cheng Y, Albanese M, Jung C, Keppler OT, and Hornung V (2020). CARD8 inflammasome activation triggers pyroptosis in human T cells. The EMBO Journal n/a, e105071. [PubMed: 32840892]

Martinon F, Burns K, and Tschopp J (2002). The Inflammasome: A Molecular Platform Triggering Activation of Inflammatory Caspases and Processing of proIL-β. Mol Cell 10, 417–426. [PubMed: 12191486]

Mastronarde DN (2005). Automated electron microscope tomography using robust prediction of specimen movements. J Struct Biol 152, 36–51. [PubMed: 16182563]

Morin A, Eisenbraun B, Key J, Sanschagrin PC, Timony MA, Ottaviano M, and Sliz P (2013). Collaboration gets the most out of software. eLife 2, e01456. [PubMed: 24040512]

Nabet B, Roberts JM, Buckley DL, Paulk J, Dastjerdi S, Yang A, Leggett AL, Erb MA, Lawlor MA, Souza A, et al. (2018). The dTAG system for immediate and target-specific protein degradation. Nature Chemical Biology 14, 431–441. [PubMed: 29581585]

Naydenova K, and Russo CJ (2017). Measuring the effects of particle orientation to improve the efficiency of electron cryomicroscopy. Nat Commun 8, 629. [PubMed: 28931821]

Okondo MC, Johnson DC, Sridharan R, Go EB, Chui AJ, Wang MS, Poplawski SE, Wu W, Liu Y, Lai JH, et al. (2016). DPP8 and DPP9 inhibition induces pro-caspase-1-dependent monocyte and macrophage pyroptosis. Nat Chem Biol 13, 46. [PubMed: 27820798]

Punjani A, Rubinstein JL, Fleet DJ, and Brubaker MA (2017). cryoSPARC: algorithms for rapid unsupervised cryo-EM structure determination. Nat Methods 14, 290–296. [PubMed: 28165473]

Punjani A, Zhang H, and Fleet DJ (2019). Non-uniform refinement: Adaptive regularization improves single particle cryo-EM reconstruction. bioRxiv, 2019.2012.2015.877092.

Qin G, Robinson K, Chenrui X, Jiawen Z, Zhi BZ, Thiam Teo DE, Yaming Z, Yew Lim JS, Ing GW, Wright G, et al. (2020). Structural basis for distinct inflammasome complex assembly by human NLRP1 and CARD8. bioRxiv, 2020.2006.2017.156307.

Robert Hollingsworth L, David L, Li Y, Griswold AR, Ruan J, Sharif H, Fontana P, Orth-He EL, Fu TM, Bachovchin DA, et al. (2021). Mechanism of filament formation in UPA-promoted CARD8 and NLRP1 inflammasomes. Nat Commun 12, 189. [PubMed: 33420033]

Robert X, and Gouet P (2014). Deciphering key features in protein structures with the new ENDscript server. Nucleic Acids Res 42, W320–324. [PubMed: 24753421]

Robinson KS, Teo DET, Tan KS, Toh GA, Ong HH, Lim CK, Lay K, Au BV, Lew TS, Chu JJH, et al. (2020). Enteroviral 3C protease activates the human NLRP1 inflammasome in airway epithelia. Science, eaay2002. [PubMed: 33093214]

Rohou A, and Grigorieff N (2015). CTFFIND4: Fast and accurate defocus estimation from electron micrographs. Journal of Structural Biology 192, 216–221. [PubMed: 26278980]

Roppongi S, Suzuki Y, Tateoka C, Fujimoto M, Morisawa S, Iizuka I, Nakamura A, Honma N, Shida Y, Ogasawara W, et al. (2018). Crystal structures of a bacterial dipeptidyl peptidase IV reveal a novel substrate recognition mechanism distinct from that of mammalian orthologues. Sci Rep 8, 2714. [PubMed: 29426867]

Ross B, Krapp S, Augustin M, Kierfersauer R, Arciniega M, Geiss-Friedlander R, and Huber R (2018). Structures and mechanism of dipeptidyl peptidases 8 and 9, important players in cellular homeostasis and cancer. Proc Natl Acad Sci USA 115, E1437–E1445. [PubMed: 29382749]

Sandstrom A, Mitchell PS, Goers L, Mu EW, Lesser CF, and Vance RE (2019). Functional degradation: A mechanism of NLRP1 inflammasome activation by diverse pathogen enzymes. Science 364, eaau1330. [PubMed: 30872533]

Scheres SH (2012). RELION: implementation of a Bayesian approach to cryo-EM structure determination. J Struct Biol 180, 519–530. [PubMed: 23000701]

Schrödinger Release 2020-1, M. (2020) (New York, NY: Schrödinger, LLC).

Shen C, Sharif H, Xia S, and Wu H (2019). Structural and mechanistic elucidation of inflammasome signaling by cryo-EM. Curr Opin Struct Biol 58, 18–25. [PubMed: 31128494]

Soler VJ, Tran-Viet KN, Galiacy SD, Limviphuvadh V, Klemm TP, St Germain E, Fournie PR, Guillaud C, Maurer-Stroh S, Hawthorne F, et al. (2013). Whole exome sequencing identifies a mutation for a novel form of corneal intraepithelial dyskeratosis. J Med Genet 50, 246–254. [PubMed: 23349227]

Spagnuolo PA, Hurren R, Gronda M, MacLean N, Datti A, Basheer A, Lin FH, Wang X, Wrana J, and Schimmer AD (2013). Inhibition of intracellular dipeptidyl peptidases 8 and 9 enhances parthenolide's anti-leukemic activity. Leukemia 27, 1236–1244. [PubMed: 23318959]

Suloway C, Pulokas J, Fellmann D, Cheng A, Guerra F, Quispe J, Stagg S, Potter CS, and Carragher B (2005). Automated molecular microscopy: the new Leginon system. J Struct Biol 151, 41–60. [PubMed: 15890530]

Tsu BV, Beierschmitt C, Ryan AP, Agarwal R, Mitchell PS, and Daugherty MD (2020). Diverse viral proteases activate the NLRP1 inflammasome. bioRxiv *doi:* 10.1101/2020.10.16.343426.

Wagner T, Merino F, Stabrin M, Moriya T, Antoni C, Apelbaum A, Hagel P, Sitsel O, Raisch T, Prumbaum D, et al. (2019). SPHIRE-crYOLO is a fast and accurate fully automated particle picker for cryo-EM. Communications Biology 2, 218. [PubMed: 31240256]

Wang C, Yu C, Ye F, Wei Z, and Zhang M (2012). Structure of the ZU5-ZU5-UPA-DD tandem of ankyrin-B reveals interaction surfaces necessary for ankyrin function. Proc Natl Acad Sci U S A 109, 4822–4827. [PubMed: 22411828]

Wang Q, Gao H, Clark KM, Mugisha CS, Davis K, Tang JP, Harlan GH, DeSelm CJ, Presti RM, Kutluay SB, et al. (2021). CARD8 is an inflammasome sensor for HIV-1 protease activity. Science, eabe1707. [PubMed: 33542150]

Wang R, Wei Z, Jin H, Wu H, Yu C, Wen W, Chan LN, Wen Z, and Zhang M (2009). Autoinhibition of UNC5b revealed by the cytoplasmic domain structure of the receptor. Mol Cell 33, 692–703. [PubMed: 19328064]

Winn MD, Ballard CC, Cowtan KD, Dodson EJ, Emsley P, Evans PR, Keegan RM, Krissinel EB, Leslie AG, McCoy A, et al. (2011). Overview of the CCP4 suite and current developments. Acta Crystallogr D Biol Crystallogr 67, 235–242. [PubMed: 21460441]

Zhang K (2016). Gctf: Real-time CTF determination and correction. J Struct Biol 193, 1–12. [PubMed: 26592709]

Zheng SQ, Palovcak E, Armache J-P, Verba KA, Cheng Y, and Agard DA (2017). MotionCor2: anisotropic correction of beam-induced motion for improved cryo-electron microscopy. Nat Meth 14, 331–332.

Zhong FL, Mamai O, Sborgi L, Boussofara L, Hopkins R, Robinson K, Szeverenyi I, Takeichi T, Balaji R, Lau A, et al. (2016). Germline NLRP1 Mutations Cause Skin Inflammatory and Cancer Susceptibility Syndromes via Inflammasome Activation. Cell 167, 187–202.e117. [PubMed: 27662089]

Zhong FL, Robinson K, Teo DET, Tan K-Y, Lim C, Harapas CR, Yu C-H, Xie WH, Sobota RM, Au VB, et al. (2018). Human DPP9 represses NLRP1 inflammasome and protects against auto-inflammatory diseases via both peptidase activity and FIIND domain binding. J Biol Chem.

Zivanov J, Nakane T, Forsberg BO, Kimanius D, Hagen WJH, Lindahl E, and Scheres SHW (2018). New tools for automated high-resolution cryo-EM structure determination in RELION-3. eLife 7, e42166. [PubMed: 30412051]

Zivanov J, Nakane T, and Scheres SHW (2020). Estimation of high-order aberrations and anisotropic magnification from cryo-EM data sets in RELION-3.1. IUCrJ 7, 253–267.

Highlights

- Cryo-EM reveals a CARD8-DPP9 ternary complex that can sequester CARD8 CT
- Binding to DPP9 is necessary for proper regulation of the CARD8 inflammasome
- DPP9 complex assembly is a checkpoint for CARD8 downstream of the proteasome
- Both N-terminal degradation and disruption of the ternary complex can activate CARD8

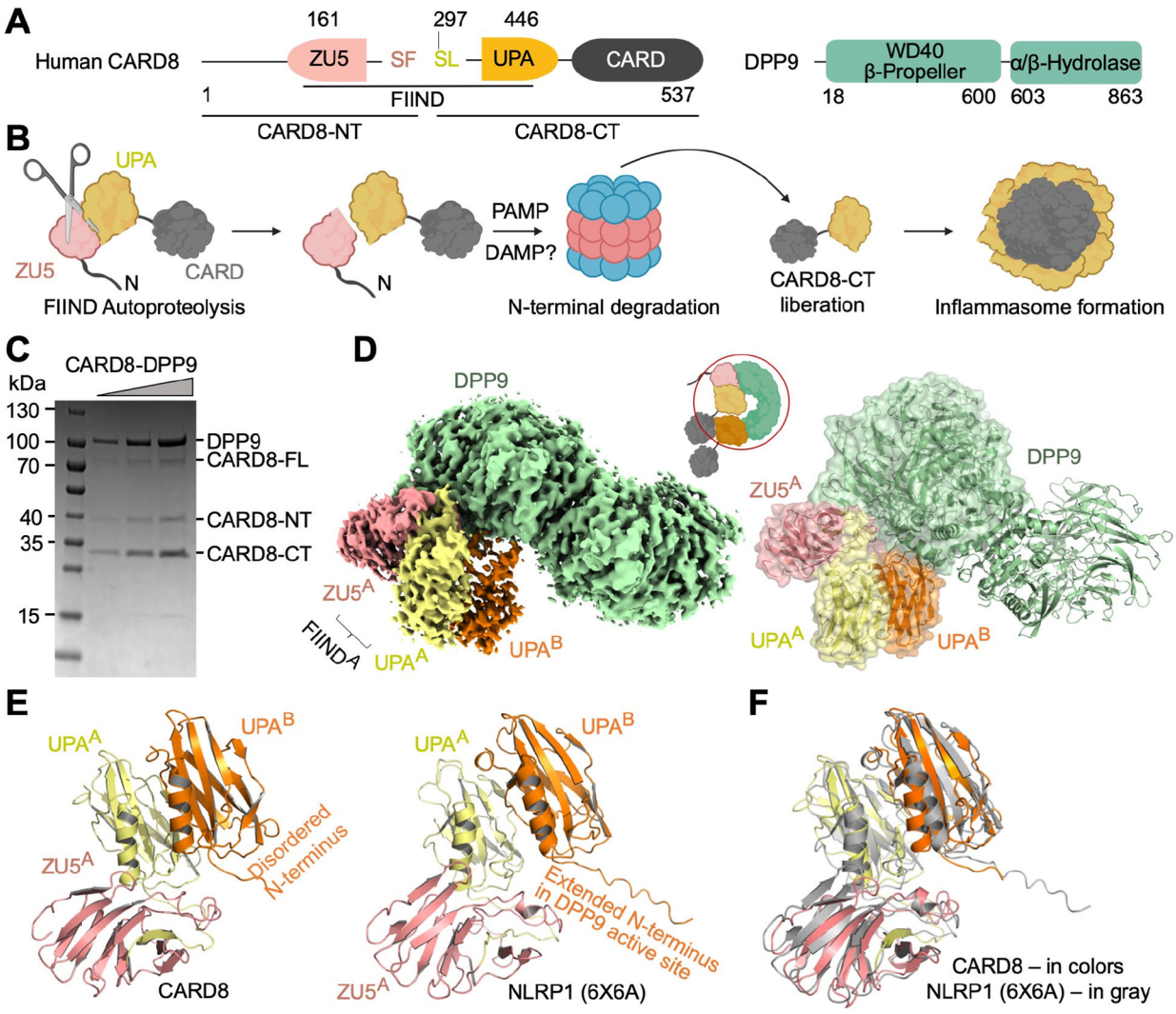

Figure 1. Cryo-EM Structure of the CARD8-DPP9 Complex.

(A) Domain architecture of CARD8 and DPP9. The FIIND autoprocessing site is between F296 and S297.

(B) Schematic diagram of CARD8 activation by N-terminal degradation.

(C) SDS-PAGE of the purified CARD8-DPP9 complex, revealing both processed and unprocessed CARD8. The CARD8-CT appears overstochiometric to the CARD8-NT.

(D) Cryo-EM density (left) and model (right) of the CARD8-DPP9 complex at a 2:2 CARD8-DPP9 stoichiometry colored as in (A). One complete ZU5-UPA pair (site A) and a second UPA (site B) associate with a DPP9 monomer. A schematic (middle) denotes the construct versus the ordered, resolved portions of the protein (red circle).

(E) Comparison of the CARD8 (left) and NLRP1 (right) $ZU5^{A}$-UPA^{A}-UPA^{B} modules. The N-terminus for NLRP1-UPA^{B} extends to bind into the DPP9 active site whereas the same segment is disordered for CARD8-UPA^{B}.

(F) Orientational difference between CARD8 (colored) and NLRP1 (grey). DPP9 dimers in the CARD8-DPP9 and NLRP1-DPP9 (6X6A) complexes were superimposed, showing the

different relative relationships between the domains. See also Figure S1 and S2, and Table S1

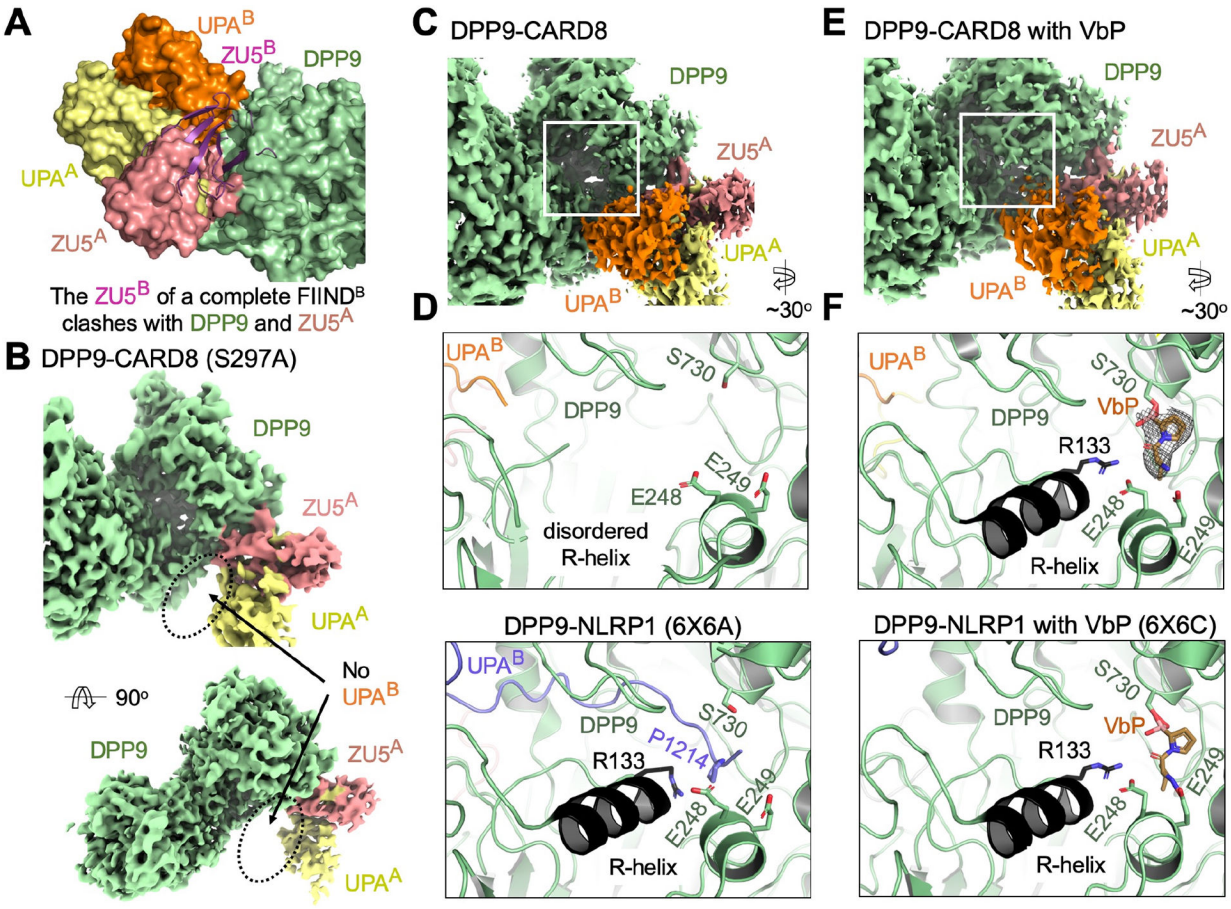

Figure 2. Binding of CARD8-CT at Site B Which is Not Disrupted by DPP9 Inhibitors.

(A) Superimposition of the ZU5^{A}-UPA^{A} relationship onto UPA^{B} to generate a theoretical ZU5^{B} (purple). A theoretical ZU5^{B} cannot be accommodated by the structure, explaining why site B is a dissociated UPA^{B}, rather than a complete FIIND.

(B) Cryo-EM density of the DPP9-CARD8 (S297A) complex with no visible UPA^{B} density. Autoproteolysis, and presumably, N-terminal degradation is required for site B association.

(C) Density of the DPP9-CARD8 complex near the DPP9 active site.

(D) Zoom-in of the DPP9 substrate tunnel in the DPP9-CARD8 complex. CARD8-UPA^{B} binds near, but not into, the DPP9 substrate tunnel and the R-helix remains disordered. In comparison, zoom-in view of the NLRP1-DPP9 complex (PDB ID: 6X6A) at the DPP9 active site shows occupancy by the NLRP1-CT peptide.

(E) Density of the DPP9-CARD8 complex with bound VbP near the active site.

(F) Zoom-in of the DPP9 substrate tunnel in the DPP9-CARD8 complex with VbP. VbP binds near the active site, causing R-helix ordering, but does not displace CARD8-UPA^{B}. in comparison, zoom-in view of the NLRP1-DPP9-VbP complex (PDB ID: 6X6C) at the DPP9 active site shows that VbP displaces the NLRP1-CT peptide.

See also Figure S3 and S4, and Table S1.

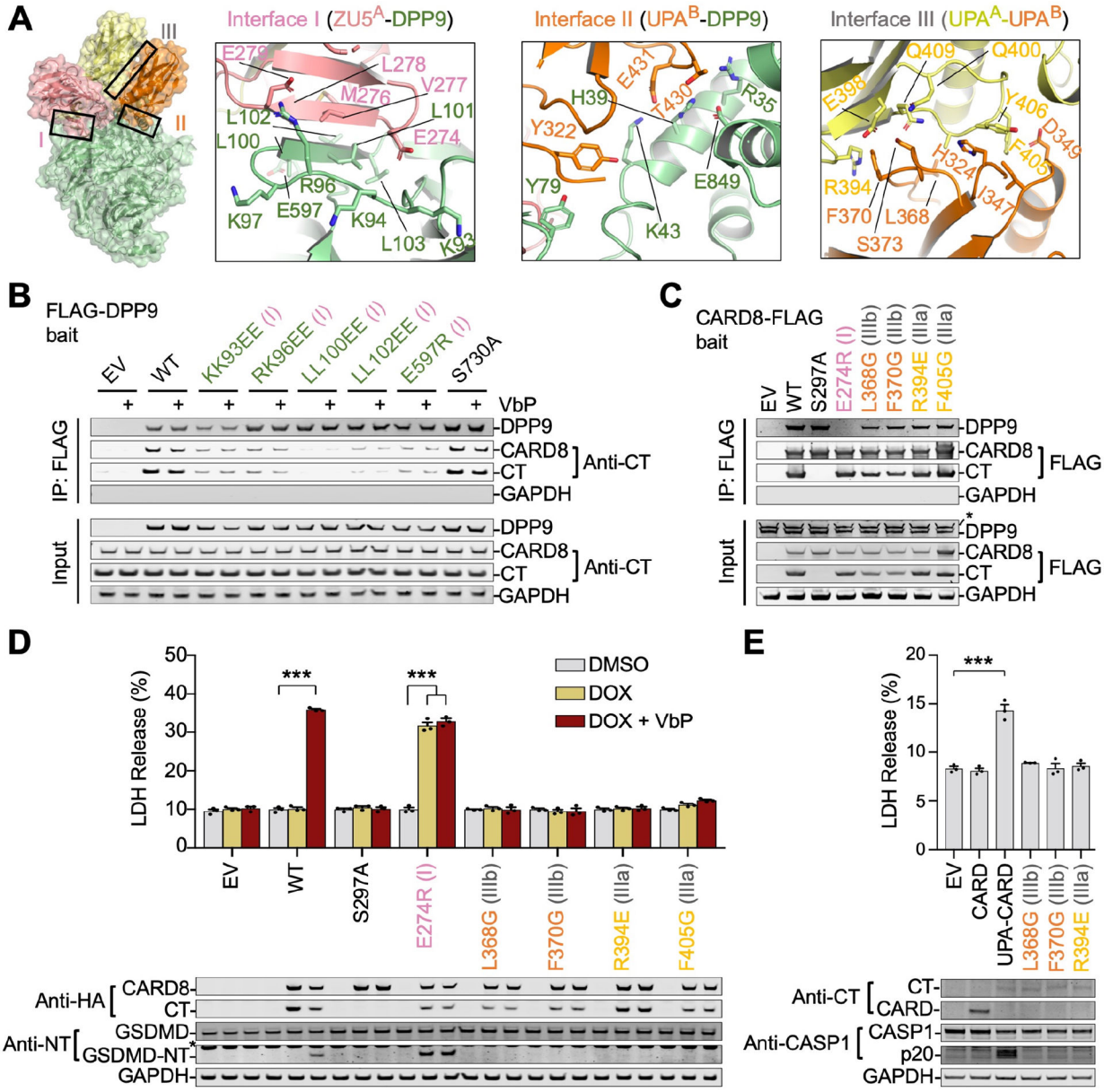

Figure 3. Mutational Analyses on the CARD8-DPP9 Interaction.

(A) Overview of interfaces I (Zu5^{A}-DPP9), II (UPA^{B}-DPP9), and III (UPA^{A}-UPA^{B}) that mediate complex assembly.

(B) FLAG co-immunoprecipitation of His-tagged CARD8 by structure-guided FLAG-tagged DPP9 mutants in the presence and absence of VbP. Constructs were expressed separately in *DPP8*$^{-/-}$ *DPP9*$^{-/-}$ HEK 293T cells and VbP was added to the combined lysates. Immunoblots are representative of 2 independent experiments.

(C) FLAG co-immunoprecipitation of endogenous DPP9 by structure-guided FLAG-tagged CARD8 mutants expressed in HEK 293T cells. The interface I mutant disrupted CARD8-DPP9 association, but the interface III mutants and the CARD8 autoprocessing-deficient mutant (S297A) did not. Immunoblots are representative of 3 independent experiments.

(D) Cell death in THP-1 *CARD8*$^{-/-}$ monocytes stably reconstituted with the indicated Tet-inducible WT and mutant FL-CARD8 constructs. Interface I mutations led to CARD8 autoactivation while interface III mutations abolished CARD8 activity as measured by LDH release (top) and Western blot (bottom) of inflammasome components. Mean ± SEM are shown from 3 independent biological replicates. *** $p < 0.001$ by 2-way ANOVA with Tukey's multiple comparison correction. * indicates non-specific band.
(E) Cell death in HEK 293T cells that stably express GSDMD and CASP-1 by transient expression of indicated CARD8-CT constructs. UPA-CARD enhanced while Interface III mutations abolished inflammasome activity as measured by LDH release (top) and Western blot (bottom) of inflammasome components. Mean ± SEM are shown from 3 independent biological replicates. *** $p < 0.001$ by Student's two-sided T-test.
See also Table S2.

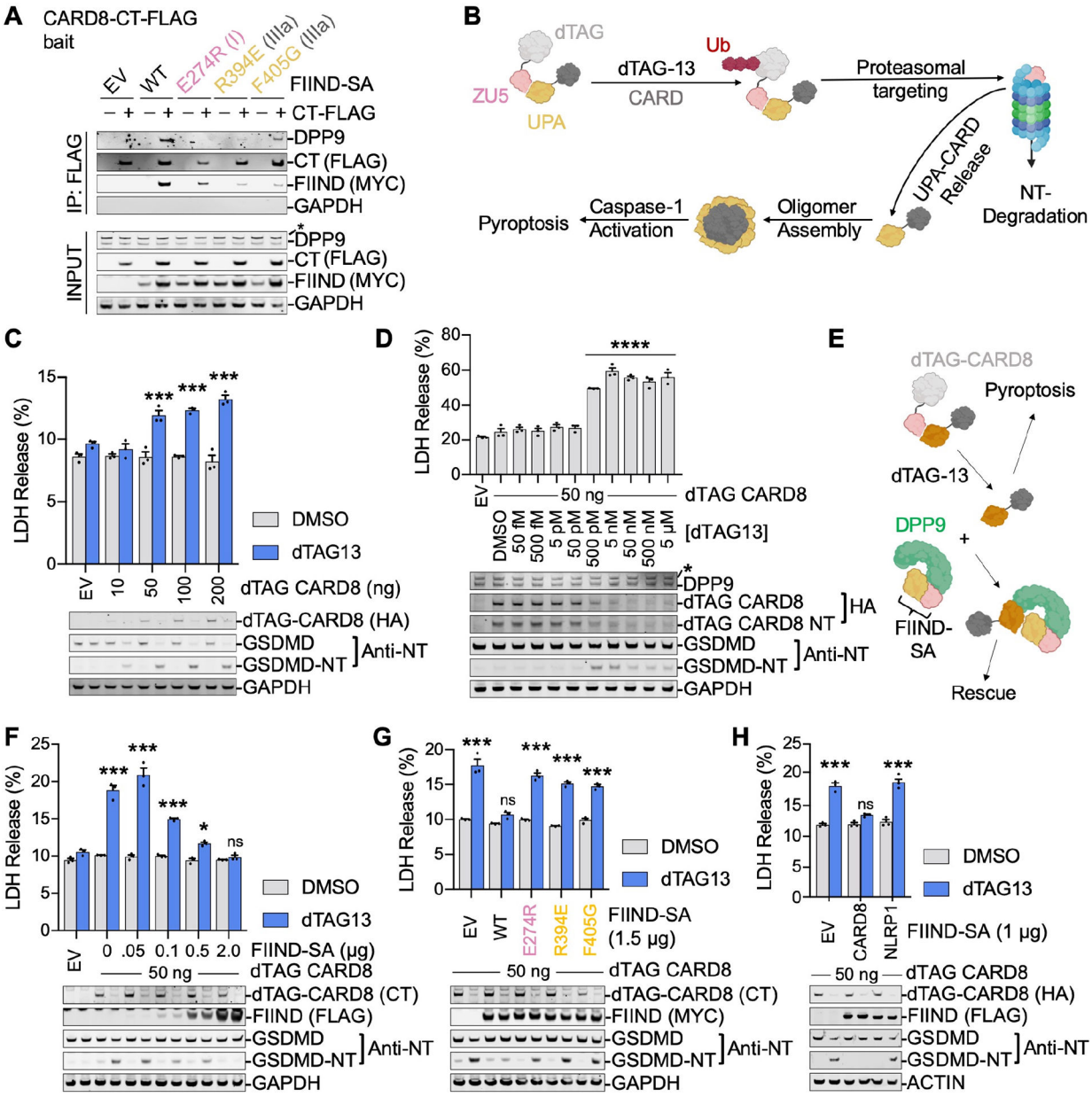

Figure 4. Suppression of CARD8-CT at Site B of DPP9 by Binding of FL-CARD8 to Site A.

(A) FLAG co-immunoprecipitation of FLAG-tagged CARD8-CT with the indicated EV (empty vector), WT and mutant CARD8-FIIND-S297A (FIIND-SA) constructs co-expressed in HEK 293T cells. The interface I mutation preserved $CARD8^{A}$-$CARD8^{B}$ interaction while abolishing DPP9 binding, and interface III mutations on FIIND-SA impaired $CARD8^{A}$-$CARD8^{B}$ interaction and the DPP9 interaction. Immunoblots are representative of 2 independent experiments. * indicates non-specific band.

(B) Schematic of the dTAG experimental system. FL-CARD8 is fused to N-terminal $FKBP12^{F36V}$ (dTAG-CARD8), which mediates ubiquitination and degradation of the fusion protein in the presence of the small molecule degrader dTAG13.

(C) Cell death induced by dTAG13 (500 nM, 3h) via N-terminal degradation in a reconstituted HEK 293T system expressing an increasing amount of dTAG-CARD8 (10–200 ng transfected plasmid). Pyroptosis was measured by LDH release (top) and GSDMD cleavage (bottom). Mean ± SEM are shown from 3 independent biological replicates. *** $p < 0.001$ compared to EV treated with DMSO by 2-way ANOVA with Tukey's multiple comparison correction.

(D) Degradation of dTAG-CARD8 is dose-dependent on the small molecule degrader, dTAG13. Pyroptosis was measured by LDH release (top) and protein content evaluated by immunoblot (bottom). Mean ± SEM are shown from 3 independent biological replicates. **** $p < 0.0001$ compared to DMSO by 1-way ANOVA with Dunnett's multiple comparison correction. * indicates non-specific band.

(E) Schematic of rescuing dTAG-13 dependent pyroptosis with the DPP9-ternary complex.

(F) Rescue of dTAG-13-induced dTAG-CARD8-mediated cell death in a HEK 293T system by increased co-expression of FIIND-SA. Pyroptosis was measured by LDH release (top) and GSDMD cleavage (bottom). dTAG-13 was used at 500 nM for 3 hr. Mean ± SEM are shown from 3 independent biological replicates. ***, * and ns denote $p < 0.001$, $p < 0.1$ and not significant, respectively, in comparison to EV treated with DMSO by 2-way ANOVA with Tukey's multiple comparison correction.

(G) Failed rescue of CARD8-CT-mediated cell death by mutant FIIND-SA constructs that abolish tertiary complex formation, measured by LDH release (top) and GSDMD processing (bottom). Reconstituted HEK 293T cells expressing dTAG-CARD8 and FIIND-SA were treated with dTAG-13 (500 nM, 3h). Mean ± SEM are shown from 3 independent biological replicates. *** and ns denote $p < 0.001$ and not significant, respectively, in comparison to EV treated with DMSO by 2-way ANOVA with Tukey's multiple comparison correction.

(H) NLRP1 does not rescue CARD8-CT mediated cell death. Reconstituted HEK 293T cells expressing dTAG-CARD8 and FIIND-SA were treated with dTAG-13 (500 nM, 3 h). Mean ± SEM are shown from 3 independent biological replicates. *** and ns denote $p < 0.001$ and not significant, respectively, in comparison to EV treated with DMSO by 2-way ANOVA with Tukey's multiple comparison correction.

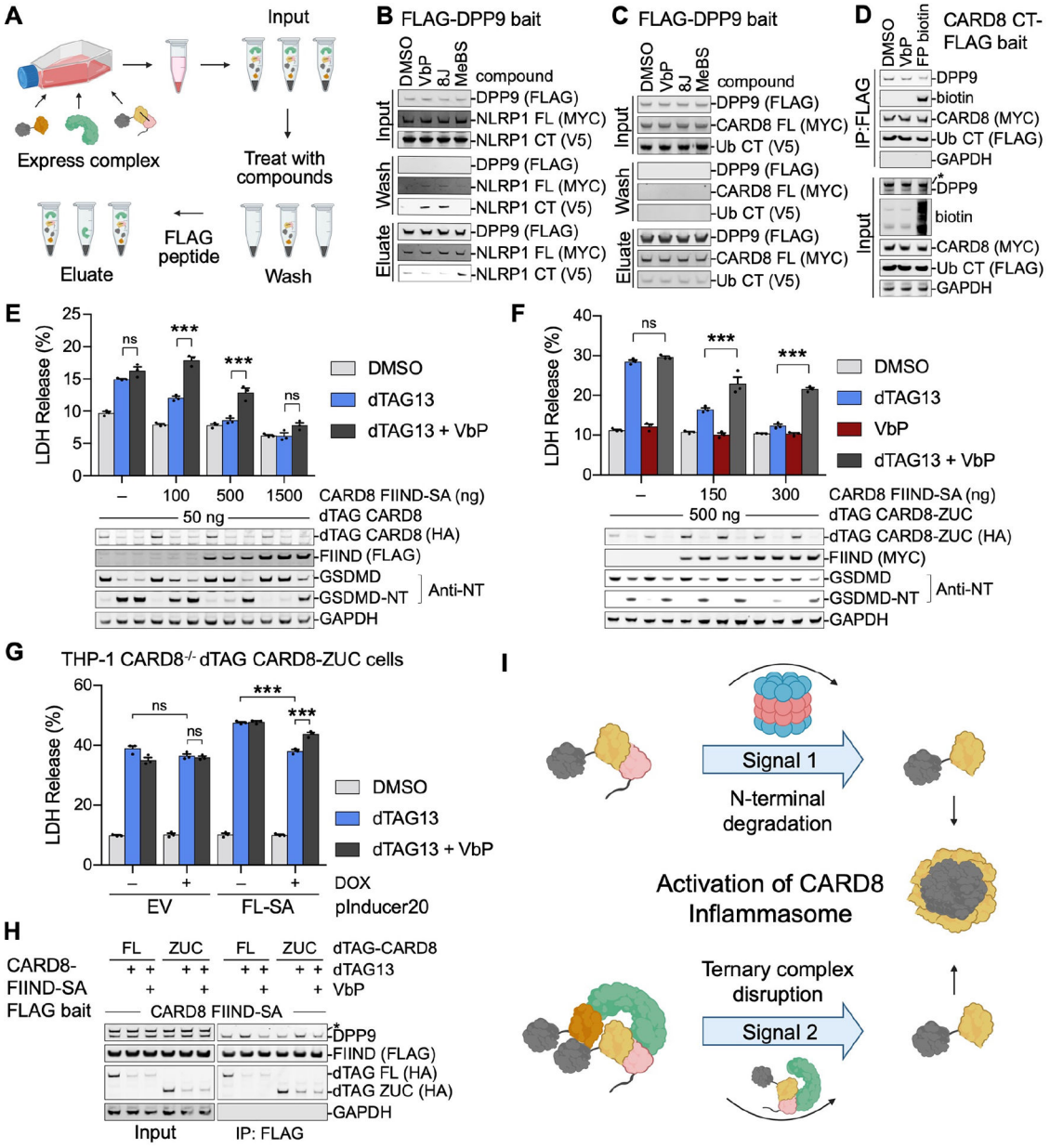

Figure 5. Two Distinct Ways to Activate the CARD8 Inflammasome

(A) Schematic of a direct displacement assay for DPP9 inhibition. Co-expressed FLAG-DPP9, NLRP1 or CARD8 CT-V5 and full-length NLRP1 or CARD8 SA mutant (FL-SA-MYC) (Input) were captured on FLAG beads. The bound components were displaced with DPP8/9 inhibitors or control compounds (Wash), and then eluted with 3x-FLAG peptide (Eluate).

(B) Displacement of NLRP1-CT from DPP9 by the DPP8/9 inhibitors VbP and 8J in vitro as depicted in (A). The displacement was apparent in the Wash, and also visible in the Eluate. The vehicle control DMSO or the non-selective aminopeptidase inhibitor MeBs did not cause displacement.

(C) Lack of displacement of CARD8-CT from DPP9 in vitro by any of the compounds. Immunoblots are representative of 2 independent experiments.
(D) FP biotin reduces capture of DPP9 by CARD8. Lysates from HEK 293T cells ectopically expressing full-length CARD8 and CARD8 CT-FLAG, were incubated with DMSO, VbP, or FP biotin prior to FLAG co-immunoprecipitation. Immunoblots are representative of 2 independent experiments.
(E) Further enhancement of cell death by VbP in dTAG13-induced CARD8 activation in the presence of FIIND-SA rescue. Reconstituted HEK 293T cells expressing dTAG-CARD8 and increasing amount of FIIND-SA were treated with dTAG-13 (500 nM) alone, or both dTAG-13 and VbP (10 μM) for 3 hr. Cell death was measured by LDH release (top) and GSDMD processing (bottom). The enhancement was most apparent at a lower dose of transfected FIIND-SA. Mean ± SEM are shown from 3 independent biological replicates. *** and ns denote $p < 0.001$ and not significant, respectively, by 2-way ANOVA with Tukey's multiple comparison correction.
(F) VbP disruption of FIIND-SA mediated cell death rescue independent of VbP-induced CARD8 degradation. Reconstituted HEK 293T cells were expressed with dTAG-CARD8-ZUC, which does not contain the N-terminal disordered sequence to undergo VbP-induced degradation, and increasing amount of FIIND-SA, and treated with dTAG-13 (500 nM), VbP (10 μM), or dTAG13 plus VbP for 3 hr. Mean ± SEM are shown from 3 independent biological replicates. * and *** denote $p < 0.05$ and $p < 0.001$, respectively, by 2-way ANOVA with Tukey's multiple comparison correction.
(G) Functional disruption of FL-SA rescue of dTAG13-induced CARD8 activation by VbP in monocytes. THP-1 *CARD8*$^{-/-}$ cells were stably reconstituted with dTAG-ZUC, with or without the Tet-inducible FL-SA (S297A) construct. While doxycycline (DOX)-dependent FL-SA expression dampened dTAG-13 induced pyroptosis, VbP disrupted this rescue. Mean ± SEM are shown from 3 independent biological replicates. *** and ns denote $p < 0.001$ and not significant, respectively, by 2-way ANOVA with Tukey's multiple comparison correction.
(H) Reduction of co-immunoprecipitated DPP9 by FLAG-tagged CARD8-FIIND-S297A (FIIND-SA). HEK 293T cells were co-expressed with FLAG-FIIND-SA and dTAG-CARD8 (FL) or dTAG-CARD8-ZUC (ZUC) constructs and treated with dTAG13 (500 nM) alone or dTAG13 plus VbP (10 μM) for 24 hr. * indicates non-specific band.
(I) Model of CARD8 inflammasome activation upstream of the proteosome (signal 1) and downstream of the proteasome (signal 2).
See also Figure S5.

KEY RESOURCES TABLE

REAGENT or RESOURCE	SOURCE	IDENTIFIER
Antibodies		
DPP9 rabbit polyclonal Ab	Abcam	ab42080
FLAG® M2 monoclonal Ab	Sigma	F3165
GAPDH rabbit monoclonal Ab	Cell Signaling Technology	14C10
CARD8 C-terminal rabbit polyclonal Ab	Abcam	ab24186
V5 rabbit polyclonal Ab	Abcam	ab9116
CASP1 rabbit polyclonal Ab	Cell Signaling Technology	2225
GSDMD rabbit polyclonal Ab	Novus	NBP2-33422
MYC tag rabbit monoclonal Ab	Cell Signaling Technology	2278
HA tag rabbit monoclonal Ab	Cell Signaling Technology	3724
Actin rabbit monoclonal Ab	Abcam	ab179467
IRDye 800CW anti-rabbit	LI-COR	925-32211
IRDye 800CW anti-mouse	LI-COR	925-32210
IRDye 680CW anti-rabbit	LI-COR	925-68073
IRDye 680CW anti-mouse	LI-COR	925-68072
IRDye 680RD streptavidin	LI-COR	926-68079
Experimental Models: Cell Lines		
Expi293F cells	ThermoFisher	A14528
HEK 293T cells	ATCC	CRL-3216
CASP1/GSDMD HEK 293T Cells	Ball et al., 2020	N/A
DPP8$^{-/-}$*DPP9*$^{-/-}$ HEK 293T Cells	Hollingsworth*, Sharif*, and Griswold* et al., 2020	N/A
DPP9$^{-/-}$ HEK 293T Cells	Griswold et al., 2019	N/A
Sf9 Cells	ThermoFisher (Gibco)	B82501
THP-1 *CARD8*$^{-/-}$ cells	Johnson* and Taabazuing* et al. 2018	N/A
THP-1 *CARD8*$^{-/-}$ + pInducer20 CARD8 cells	This paper	N/A
THP-1 *CARD8*$^{-/-}$ + pInducer20 CARD8 S297A cells	This paper	N/A
THP-1 *CARD8*$^{-/-}$ + pInducer20 CARD8 E274R cells	This paper	N/A
THP-1 *CARD8*$^{-/-}$ + pInducer20 CARD8 L368G cells	This paper	N/A
THP-1 *CARD8*$^{-/-}$ + pInducer20 CARD8 F370G cells	This paper	N/A
THP-1 *CARD8*$^{-/-}$ + pInducer20 CARD8 R394E cells	This paper	N/A
THP-1 *CARD8*$^{-/-}$ + pInducer20 CARD8 F405G cells	This paper	N/A
THP-1 *CARD8*$^{-/-}$ + N-dTAG-CARD8 ZUC cells	This paper	N/A

REAGENT or RESOURCE	SOURCE	IDENTIFIER
THP-1 *CARD8*$^{-/-}$ + pInducer20 CARD8 S297A + N-dTAG-CARD8 ZUC cells	This paper	N/A
Chemicals, Peptides, and Recombinant proteins		
TCEP-HCL	GoldBio	TCEP1
DTT	GoldBio	DTT10
Trizma® base	Millipore Sigma	T1503
HEPES	Millipore Sigma	H3375
PBS, pH 7.4	Millipore Sigma	P3813
Sodium Chloride	Millipore Sigma	S5886
Glutaraldehyde solution	Millipore Sigma	G5882
4x Laemmli Sample Buffer	BIO-RAD	1610747
45% Glucose, sterile-filtered	Millipore Sigma	G8769
Sodium valproic acid	Millipore Sigma	P4543
Val-boroPro (talabostat) mesylate	Cayman	29007
dTAG-13	Tocris	6605
Fluorophosphonate PEG23 biotin (FP-biotin)	Griswold et al., 2019.	N/A
bestatin methyl ester (Me-Bs)	Sigma	200485
Compound 8J	Van Goethem, S. et al.	N/A
Polyethylenimine	Polysciences	23966-1
Lipofectamine2000	Invitrogen	12566014
Fugene HD	Promega	E2311
Cellfectin II	ThermoFisher	10362100
TEV protease	Hao Wu Lab	N/A
HRV 3C protease	Hao Wu Lab	N/A
3X FLAG® peptide	Sigma	F4799
Uranyl formate hydrate	Electron Microscopy Sciences	22450
Software and Algorithms		
cryoSPARC v2.15.0	Punjani et al. 2017, Punjani et al., 2019	https://cryosparc.com/
RELION v3.08 and 3.1	Scheres and Chen, 2012 Zivanov*, Nakane*, and Forsberg* et al., 2019	https://www3.mrc-lmb.cam.ac.uk/relion//index.php?title=Main_Page
crYOLO	Wagner et al., 2019.	https://sphire.mpg.de/wiki/doku.php?id=pipeline:window:cryolo
SerialEM	Mastronarde, D.N. 2005.	https://bio3d.colorado.edu/SerialEM/
Leginon	Suloway et al., 2005	https://emg.nysbc.org/redmine/projects/leginon/wiki/Leginon_Homepage
EPU	ThermoFisher	https://www.fei.com/software/epu-automated-single-particles-software-for-life-sciences/
Gctf	Zhang, K. 2016	https://www.mrc-lmb.cam.ac.uk/kzhang/
CTFFIND4	Rough and Grigorieff, 2015	https://grigoriefflab.umassmed.edu/ctffind4
MotionCor2	Zheng et al., 2017	https://emcore.ucsf.edu/ucsf-motioncor2
GemSPOT	Robertson et al., 2020	https://github.com/mjrober101/GemSpot

REAGENT or RESOURCE	SOURCE	IDENTIFIER
Maestro	Schrodinger	https://www.schrodinger.com/maestro
Jaguar	Schrodinger	https://www.schrodinger.com/jaguar
Prime	Schrodinger	https://www.schrodinger.com/prime
Glide	Schrodinger	https://www.schrodinger.com/glide
Phenix	Liebschner et al. 2019	https://www.phenix-online.org
Coot	Emsley et al., 2010	https://www2.mrc-lmb.cam.ac.uk/personal/pemsley/coot/
ResMAP	Kucukelbir et al. 2014	http://resmap.sourceforge.net
UCSF Chimera	Goddard et al., 2007	https://www.rbvi.ucsf.edu/chimera/
UCSF ChimeraX	Goddard et al., 2018	https://www.rbvi.ucsf.edu/chimerax/
Pymol	Schrodinger	https://pymol.org/2/
DALI	Holm 2019	http://ekhidna2.biocenter.helsinki.fi/dali/
ESPript v3.0	Robert and Gouet 2014	http://espript.ibcp.fr/ESPript/ESPript/
Graphpad prism v7	Graphpad	https://www.graphpad.com/scientific-software/prism/
BioRender	BioRender	https://biorender.com/
SBgrid	Morin et al,, 2013	https://sbgrid.org/
Deposited Data		
CryoEM maps	This paper	CARD8-DPP9: EMD-22367 CARD8-DPP9-VbP: EMD-22402 CARD8-S297A-DPP9: EMD-22974
Atomic models	This paper	CARD8-DPP9 PDB ID: 7JKQ CARD8-DPP9-VbP PDB ID: 7JN7
Raw EM data	This paper	CARD8-DPP9: EMPIAR-10597 CARD8-DPP9-VbP: EMPIAR-10596 CARD8-S297A-DPP9: EMPIAR-10600
Extended protocols	This paper	https://www.protocols.io/groups/hao-wu-lab
Pymol sessions, additional data	This paper	https://osf.io/x7dv8/
Vectors and plasmids		
pFastBac HTB	ThermoFisher	10584027
pFastBac LIC 4B	Scott Gradia	Addgene #30115
pcDNA3.1 LIC 6A vector	Scott Gradia	Addgene #30124
pcDNA3.1 LIC 6D vector	Scott Gradia	Addgene #30127
pInducer20 CARD8-HA PAM	This paper	Addgene #169982
pcDNA3.1-TEV-GFP-FLAG LIC cloning vector (6LD)	Hollingsworth*, Sharif*, and Griswold* et al., 2020	Addgene #166835
pcDNA 3.1 His-TEV-CARD8	This paper	By request
pcDNA3.1 CARD8-TEV-GFP-FLAG	This paper	Addgene #169991
pcDNA3.1 CARD8-TEV-GFP-FLAG S297A	This paper	Addgene #169992
pInducer20 CARD8-HA PAM	This paper	Addgene #169982
pInducer20 CARD8-HA PAM S297A	This paper	Addgene #169983
pInducer20 CARD8-HA PAM E274R	This paper	Addgene #169984
pInducer20 CARD8-HA PAM L368G	This paper	Addgene #169985

REAGENT or RESOURCE	SOURCE	IDENTIFIER
pInducer20 CARD8-HA PAM F370G	This paper	Addgene #169986
pInducer20 CARD8-HA PAM R394E	This paper	Addgene #169987
pInducer20 CARD8-HA PAM F405G	This paper	Addgene #169988
pcDNA3.1 Ub-S297 CARD8 WT	This paper (Genscript)	Addgene #169958
pcDNA3.1 Ub-S297 CARD8 L368G	This paper (Genscript)	Addgene #169959
pcDNA3.1 Ub-S297 CARD8 F370G	This paper (Genscript)	Addgene #169960
pcDNA3.1 Ub-S297 CARD8 R394E	This paper (Genscript)	Addgene #169961
pfastBac HTB His-TEV-DPP9S	Hollingsworth*, Sharif*, and Griswold* et al., 2020	Addgene #166787
pFastBac HTB DPP9S S730A	This paper	Addgene #169946
pFastBac HTB DPP9S D808N	This paper	Addgene #169947
pcDNA3.1 LIC 6A Flag-TEV-DPP9S	Hollingsworth*, Sharif*, and Griswold* et al., 2020	Addgene #166794
pcDNA3.1 LIC 6A Flag-TEV-DPP9S S730A	Hollingsworth*, Sharif*, and Griswold* et al., 2020	Addgene #166801
pcDNA3.1 LIC 6A Flag-TEV-DPP9S KK93EE	Hollingsworth*, Sharif*, and Griswold* et al., 2020	Addgene #166796
pcDNA3.1 LIC 6A Flag-TEV-DPP9S RK96EE	Hollingsworth*, Sharif*, and Griswold* et al., 2020	Addgene #166797
pcDNA3.1 LIC 6A Flag-TEV-DPP9S LL100EE	Hollingsworth*, Sharif*, and Griswold* et al., 2020	Addgene #166798
pcDNA3.1 LIC 6A Flag-TEV-DPP9S LL102EE	Hollingsworth*, Sharif*, and Griswold* et al., 2020	Addgene #166799
pcDNA3.1 LIC 6A Flag-TEV-DPP9S E597R	Hollingsworth*, Sharif*, and Griswold* et al., 2020	Addgene #166800
pcDNA3.1 LIC 6A CARD8 Ub-S297-FLAG F405G	This paper	Addgene #170119
pcDNA3.1 LIC 6A CARD8-FLAG	This paper	Addgene #169948
pcDNA3.1 LIC 6A CARD8-FLAG S297A	This paper	Addgene #169949
pcDNA3.1 LIC 6A CARD8-FLAG E274R	This paper	Addgene #169950
pcDNA3.1 LIC 6A CARD8-FLAG E274R + S297A	This paper	Addgene #169951
pcDNA3.1 LIC 6A CARD8-FLAG L368G	This paper	Addgene #169952
pcDNA3.1 LIC 6A CARD8-FLAG F370G	This paper	Addgene #169953
pcDNA3.1 LIC 6A CARD8-FLAG R394E	This paper	Addgene #169954
pcDNA3.1 LIC 6A CARD8-FLAG R394E + S297A	This paper	Addgene #169955
pcDNA3.1 LIC 6A CARD8-FLAG F405G	This paper	Addgene #169956
pcDNA3.1 LIC 6A CARD8-FLAG F405G + S297A	This paper	Addgene #169957
pcDNA3.1 LIC 6A CARD8 Ub-S297-FLAG	This paper	Addgene #169958
pcDNA3.1 LIC 6A CARD8 Ub-S297-FLAG L368G	This paper	Addgene #169959
pcDNA3.1 LIC 6A CARD8 Ub-S297-FLAG F370G	This paper	Addgene #169960

REAGENT or RESOURCE	SOURCE	IDENTIFIER
pcDNA3.1 LIC 6A CARD8 Ub-S297-FLAG R394E	This paper	Addgene #169961
pLEX305-N-dTAG-CARD8	This paper	Addgene #169989
pLEX305-N-dTAG-CARD8-ZUC	This paper	Addgene #169990
pLEX307 Ub-S297 CARD8 WT-V5	This paper	By request
pLEX307 NLRP1 S1213A MYC	This paper	By request
pLEX307 Ub-S1213 NLRP1-V5	This paper	By request
pDONR221 CARD8	This paper	Addgene #169962
pDONR221 CARD8 FIIND	This paper	Addgene #169963
pDONR221 CARD8 ZUC	This paper	Addgene #169964
pDONR221 CARD8 Ub-S297	This paper	Addgene #169965
pDONR221 CARD8 FIIND S297A	This paper	Addgene #169966
pDONR221 CARD8 FIIND E274R	This paper	Addgene #169967
pDONR221 CARD8 FIIND E274R + S297A	This paper	Addgene #169968
pDONR221 CARD8 FIIND L368G	This paper	Addgene #169969
pDONR221 CARD8 FIIND L370G	This paper	Addgene #169970
pDONR221 CARD8 FIIND R394E	This paper	Addgene #169971
pDONR221 CARD8 FIIND R394E + S297A	This paper	Addgene #169972
pDONR221 CARD8 FIIND F405G	This paper	Addgene #169973
pDONR221 CARD8 FIIND F405G + S297A	This paper	Addgene #169974
pDONR221 CARD8 PAM	This paper	Addgene #169975
pDONR221 CARD8 PAM S297A	This paper	Addgene #169976
pDONR221 CARD8 PAM E274R	This paper	Addgene #169977
pDONR221 CARD8 PAM L368G	This paper	Addgene #169978
pDONR221 CARD8 PAM F370G	This paper	Addgene #169979
pDONR221 CARD8 PAM R394E	This paper	Addgene #169980
pDONR221 CARD8 PAM F405G	This paper	Addgene #169981
pInducer20 CARD8-HA PAM	This paper	Addgene #169982
pLEX307 NLRP1 FIIND S1213A-FLAG	Hollingsworth*, Sharif*, and Griswold* et al., 2020	By request
Other		
Anti-FLAG M2 affinity gel	Millipore Sigma	A2220
Econo-Pac® Chromatography Column	BIO-RAD	7321010
Amicon Ultra 50 kDa cutoff, 15 mL	Millipore Sigma	UFC905096
Amicon Ultra 100 kDa cutoff, 15 mL	Millipore Sigma	UFC910096
Amicon ultra 10 kDa cutoff, 0.5 mL	Millipore Sigma	UFC5010BK
Amicon ultra 50 kDa cutoff, 0.5 mL	Millipore Sigma	UFC5050BK
Amicon ultra 100 kDa cutoff, 0.5 mL	Millipore Sigma	UFC5100BK
Slide-A-Lyzer, 10 kDa cutoff, 2 mL	Millipore Sigma	88404
MonoQ 5/50 GL column	Cytiva	GE17-5166-01

REAGENT or RESOURCE	SOURCE	IDENTIFIER
Superdex 200 increase 10/300 GL column	Cytiva	28990944
Superose 6 increase 10/300 GL column	Cytiva	29091596
4–15% Mini-PROTEAN® TGX™ Precast Protein Gels	BIO-RAD	4561086
iBlot™ 2 Transfer Stacks, PVDF	Invitrogen	IB24002
iBlot™ 2 Transfer Stacks, nitrocellulose	Invitrogen	IB23001
NuPAGE™ 4–12% Bis-Tris Midi Protein Gels	Invitrogen	WG1403A
Odyssey® Blocking Buffer (PBS)	LI-COR	927-40010
DC Protein Assay kit	BIO-RAD	5000112
Quantifoil 1.2/1.3 CU200 cryo-EM grids	Electron Microscopy Sciences	Q2100CR1.3
Quantifoil 1.2/1.3 AU400 cryo-EM grids	Electron Microscopy Sciences	Q4100AR1.3
C-Flat-1.2/1.3-4C	Electron Microscopy Sciences	CF413-50
Formvar/Carbon 400 Mesh, Cu grids	Electron Microscopy Sciences	FCF400-Cu
CyQUANT™ LDH Cytotoxicity Assay Kit	ThermoFisher	C20300